SUPPORTING INFORMATION

Active site switching on high entropy phosphides as bifunctional oxygen electrocatalysts for rechargeable/robust Zn-Air battery

Ren He[a,b,‡], Shiqi Wang[c,‡], Linlin Yang[a,b,‡], Sharona Horta[d], Yang Ding[e,f], Chong Di[e], Xuesong Zhang[g], Ying Xu[e], Maria Ibáñez[d], Yingtang Zhou[h], Stefan Mebs[i], Holger Dau[i], Jan Niklas Hausmann[j,*], Wenyi Huo[k,l,*], Prashanth W. Menezes[j,m,*], and Andreu Cabot[a,n,*]

[a.] *Catalonia Energy Research Institute – IREC, Sant Adria de Besòs, 08930 Barcelona, Spain.*

[b.] *Enginyeria Electrònica i Biomèdica Facultat de Física, Universitat de Barcelona, 08028 Barcelona, Spain.*

[c.] *Jiangsu Key Laboratory of Advanced Metallic Materials, Southeast University, Nanjing 211189, China.*

[d.] *Institute of Science and Technology Austria, Am Campus 1, 3400, Klosterneuburg, Austria.*

[e.] *Hebei Key Lab of Optic-electronic Information and Materials, College of Physics Science and Technology, Hebei University, Baoding, 071002, China.*

[f.] *Songshan lake materials laboratory, Dongguan,523820, China.*

[g.] *Institut de Ciència de Materials de Barcelona (ICMAB-CSIC), Campus de la UAB, 08193 Bellaterra, Spain.*

[h.] *National Engineering Research Center for Marine Aquaculture, Marine Science and Technology College, Zhejiang Ocean University, Zhoushan, Zhejiang Province, 316004, China*

[i.] *Department of Physics, Freie Universität Berlin, Arnimallee 14, 14195 Berlin, Germany.*

[j.] *Materials Chemistry Group for Thin Film Catalysis – CatLab, Helmholtz-Zentrum Berlin für Materialien und Energie, Albert-Einstein-Str. 15, 12489 Berlin, Germany.*

[k.] *College of Mechanical and Electrical Engineering, Nanjing Forestry University, Nanjing, 210037, China.*

[l.] *NOMATEN Centre of Excellence, National Centre for Nuclear Research, Otwock, 05-400, Poland.*

[m.] *Department of Chemistry, Technische Universität Berlin, Straße des 17 Juni 135, Sekr. C2, 10623 Berlin, Germany.*

[n.] *ICREA, Pg. Lluis Companys 23, 08010, Barcelona, Catalonia, Spain*

‡ *These authors contributed equally to this work*

* *Corresponding authors: Dr. J. N. Hausmann (niklas.hausmann@helmholtz-berlin.de), Dr. W. Y. Huo (wyhuo@njfu.edu.cn), Dr. P. W. Menezes (prashanth.menezes@mailbox.tu-berlin.de) and Prof. A. Cabot (acabot@irec.cat)*

1 Experimental

1.1 Materials

Chemicals: Hexadecylamine (HDA, 90%, technical grade), triphenylphosphite (TPP, 97%), iron pentacarbonyl ($Fe(CO)_5$, ≥99.99% trace metals basis), cobalt carbonyl ($Co_2(CO)_8$, ≥90% (Co)), tungsten hexacarbonyl ($W(CO)_6$, 97%), palladium(II) acetylacetonate ($Pd(acac)_2$, 96%), ammonium chloride (NH_4Cl, ≥99.5%), ammonium thiocyanate (NH_4SCN, ≥99%) oleylamine (OAm, >70%), and Nafion solution (Sigma，5 wt%) were bought from Sigma-Aldrich. Methanol (99%), 1-octadecene (ODE, 90%), nickel(II) acetylacetonate ($Ni(acac)_2$, 96%), potassium hydroxide (KOH, 85%), and cyclohexane (99%) were supplied by Alfa Aesar. Deionized (DI) water (≥18.2 MΩ/cm) was purified by an ultra-pure purification system (Aqua Solutions).

1.2 Methods

Preparation of FeCoNiPdWP, FeCoNiPdP FeCoNiWP, FeCoPdWP, FeNiPdWP, and CoNiPdWP nanoparticles: All synthesis processes were conducted using a standard vacuum/argon Schlenk line. In a typical preparation of FeCoNiPdWP nanoparticles, 2.4 g of 1-hexadecylamine as a surfactant was combined with 10.0 mL of 1-octadecene and 2.6 mL of triphenyl phosphite in a 100 mL three-neck flask. The system was degassed and heated to 150 °C, maintained at this temperature for 1 hour to remove low-boiling-point impurities, moisture, and oxygen. Subsequently, 102.8 mg (0.4 mmol) of $Ni(acac)_2$, 0.2 mmol of $Co_2(CO)_8$, 98 mg (0.5 mmol) of $Fe(CO)_5$ (Sigma Aldrich), 140.8 mg (0.4 mmol) of $W(CO)_6$, 122 mg (0.4 mmol) of $Pd(acac)_2$, and 65 mg (1.2 mmol) of ammonium chloride were dissolved in 8 mL of ODE and 8 mL of OAm to create a homogeneous solution through ultrasonication for 1 hour, followed by degassing with argon for another hour. Afterward, the degassed homogeneous solution was transferred into a three-neck flask. It was first vacuumed for 20 minutes at 70 ºC and then the temperature was increased to 290 ºC in 15 minutes under an argon atmosphere while being stirred magnetically. The mixture was allowed to react at 290 ºC for 1 hour. Subsequently, the mixture was cooled down to 220 °C by removing the heating mantle and then rapidly cooled to room temperature with a water bath. The black product was isolated by precipitation with acetone. To remove as many organic compounds as possible, three cycles of redispersion and precipitation were carried out using chloroform and ethanol. To further eliminate the organic

ligands, the crude FeCoNiPdWP nanoparticles dispersion in 20 mL of hexane. Then, 5 mL of NH_4SCN solution in methanol (50 mmol/L) was added to form a two-phase mixture, which was agitated for 5 minutes until the nanoparticles completely mixed with the ammonium thiocyanide solution. The surface-modified nanoparticles were washed with ethanol three times and dried in a vacuum oven for 12 hours at 60 °C.

1.3 Material characterization

Scanning electron microscopy (SEM) images and energy dispersive spectroscopy (EDS) spectra were obtained in a Zeiss Auriga field emission scanning electron microscope. Transmission electron microscopy (TEM) micrographs were obtained in a Tecnai F20 field emission gun microscope with a 0.19 nm point-to-point resolution at 200 kV. Images were analyzed using Gatan Digital Micrograph software. High angle annular dark-field (HAADF)-scanning transmission electron microscopy (STEM) images and elemental mapping were measured in a spherical aberration-corrected transmission electron microscope FEI Titan G2 80-200 ChemiSTEM with four energy-dispersive X-ray spectroscopy (EDX) detectors were operated at 80 and 200 keV. The spherical aberration-corrected high-resolution transmission electron microscope (AC-HRTEM) image was obtained by spherical Aberration Corrected Transmission Electron Microscope: ACTEM (EM-ARM200F, Japan). The crystal structure was characterized by powder X-ray diffraction (XRD) measurement in a Bruker AXS D8 Advance X-ray diffractometer. (Cu-Kα radiation, λ =1.5418 Å, 40 kV and 40 mA; Bruker, Germany). Inductively coupled plasma-optical emission spectroscopy (ICP-OES) was conducted on an ICPE-9820 system. X-ray photoelectron spectroscopy (XPS) was performed with an Al anode XR50 source on a Specs system equipped with a Phoibos 150 MCD-9 detector (150 W).

In situ Raman spectra were collected by a Raman microscope (iHR320 monochromator, HORIBA) using an *in situ* Raman cell. The excitation source was a frequency-doubled Nd: YAG laser, 532 nm laser, and the spectra were collected using a grating of 1800 lines/ mm. The electrode was first subjected to chronoamperometry measurements at a set applied voltage (1.0-1.6 V vs. RHE) for 5 min, then we started acquiring Raman spectra while keeping the chronoamperometry measurements running. The Raman spectra were obtained with an acquisition time of 20 s and accumulation of 8 times from the range of 200-900 cm^{-1}.

The (quasi *in situ*) X-ray absorption near edge structure (XANES) and extended X-ray absorption fine structure (EXAFS) spectra were collected at the BESSY II synchrotron radiation source of the Helmholtz-Zentrum Berlin. The experiments were performed at the KMC-3 bending-magnet beamline at 20 K in a closed-cycle helium cryostat (Oxford). A Si(111) double-crystal monochromator was utilized to select the incident beam energy. Iron, cobalt, and nickel K-edge XAS spectra were collected in fluorescence mode using a 13-element energy-resolving silicon-drift detector (RaySpec). The K-edge energy was determined using the integral method.[1,2] The obtained spectra were weighted by k^3 and simulated in k-space (E_0(Fe) = 7112 eV, E_0(Co) = 7709 eV, E_0(Ni) = 8333 eV). EXAFS simulations were performed with in-house software after calculating the phase functions with the FEFF program (version 8.4).[3,4] The EXAFS simulations were optimized by minimization of the error sum acquired by summation of the squared deviations between experimental Fourier backtransforms in a 1-3.5 Å range of reduced distances and simulated spectra (least-squares fit using the Levenberg-Marquardt algorithm). Further details are given elsewhere.[5,6] Binder-free films (1×1 cm^2, 0.1 mg/cm^2 loading) for XAS experiments were prepared on fluorine-doped tin oxide glass substrates using electrophoretic deposition. Electrophoretic deposition was performed in a two-electrode setup (both fluorine-doped tin oxide glass) at 10 V for 1 min. The electrolyte was 8 mL acetone solution with 2 mg iodine and 30 mg sample that was sonicated before for 2 h together. Through keto-enol tautomerisation and subsequent reaction, the acetone and iodine form protons that create a surface charge on the high entropy phosphide nanoparticles. These charge particles move and deposit on the cathode during the electrophoretic deposition. This procedure has previously been described in more detail.[7–9]

1.4 Electrochemical measurements

All the electrochemical measurements were carried out on a Chi760E electrochemical workstation (Shanghai Chenhua, China) at room temperature using a standard three-electrode setup system with a platinum grid as the counter electrode, a Hg/HgO electrode as the reference electrode, and a glassy carbon (GC) as the working electrode. The catalytic ink was prepared with 4 mg of catalyst, 2 mg carbon black, and 30 µL of 5 wt% Nafion solution dispersion in 750 µL isopropanol and 220 µL deionized water with a continuous sonication until

a homogeneous solution. Then, 10 μL catalyst ink was uniformly loaded on the surface of the polished GC electrode, and dried at room temperature. All measured potentials ($E_{Hg/Hgo}$) were converted to the reversible hydrogen electrode (RHE) potential through the Nernst equation ($E_{RHE} = E_{Hg/Hgo} + 0.0591 \times pH + 0.098$), in which the PH value obtained by a PH meter (pH & Ion-metro GLP 22-Crison Instruments) is 13.85 for 1.0 M KOH electrolyte and 12.96 for 0.1 M KOH electrolyte. These values are close to the theoretically expected ones.[10]

The oxygen evolution reaction (OER) measurements were conducted in a 1.0 M KOH electrolyte. Linear sweep voltammetry (LSV) measurements were conducted at a scan rate of 5 mV/s, and then the Tafel slopes were calculated from the LSV curves. Electrochemical impedance spectroscopy (EIS) measurements were recorded at 1.5 V vs. RHE with frequencies from 0.01 to 10^5 Hz. The double-layer capacitance (C_{dl}) value was measured from cyclic voltammetry (CV) curves at different scan rates (20, 40, 80, 120, 160, 200 mV/s) within the non-faradaic potential range of 1.01–1.11 V vs. RHE. The stability was measured by chronoamperometry (CA) with carbon paper as the working electrode.

The oxygen reduction reaction (ORR) measurements were conducted in 0.1 M KOH electrolyte. A rotating ring disk electrode (RRDE) was used as the substrate for the working electrode. CV curves were measured in an O_2-saturated or Ar-saturated electrolyte at a scan rate of 10 mV/s. LSV curves were conducted in an O_2-saturated electrolyte at different rotation rates from 400-2500 rpm at a scan rate of 10 mV/s.

The hydrogen peroxide yield (H_2O_2 %) and the apparent number of electrons transferred during ORR were determined by the following equation:

$$H_2O_2(\%) = 200 \times \frac{\frac{I_r}{N}}{I_d + \frac{I_r}{N}}$$

$$n = 4 \times \frac{I_d}{I_d + \frac{I_r}{N}}$$

Here, I_r is the ring current, I_d is the disk current, and N is the H_2O_2 collection coefficient.

1.5 Zinc-air battery (ZAB) evaluation

Aqueous ZABs were assembled with a hydrophobic carbon paper with a catalytic mass loading of 0.5 mg cm^{-2} as the air cathode, a polished Zn foil as the anode, and 6 M KOH and 0.2 M zinc acetate aqueous solution as the electrolyte. The electrochemical measurement of ZABs was carried out on a CHi760E electrochemical station (Shanghai Chenhua, China). The galvanostatic test was performed using a Neware BTS4008 battery test system at room temperature. The specific capacities were determined using the galvanostatic discharge profiles standardized to the consumed mass of Zn.

1.6 DFT calculations

DFT calculations were performed using the CASTEP packages.[11] The generalized gradient approximation (GGA) exchange-correlation functionals were used to describe the electronic exchange and correlation effects.[12] We selected the ultrasoft pseudopotentials and set the plane-wave basis cutoff energy to 380 eV for all the geometry optimizations. The empirical dispersion correction in Grimme's scheme was employed to consider the van der Waals (vdW) interaction. The Liner Broyden-Fletcher-Goldfarb-Shannon (LBFGS) algorithm with the medium quality setting of k-points has been used for all the energy minimizations in this work. The geometry optimization within the conjugate gradient method was performed with forces on each atom less than 0.05 eV/Å. An energy tolerance of 5.0×10^{-5} eV per atom and a maximum displacement of 0.005Å were considered.

To understand the role of the oxyhydroxide over the reconstructed surface during the OER cycles, a FeOOH structure with (101) lattice plane was chosen as the pristine host matrix to perform DFT simulations. It is reasonable to choose the oxyhydroxide matrix due to the above HRTEM/*in-situ* Raman/XAS results and because it has been reported to be the active phase for OER catalysis. In addition, the (101) terminated surface (with H) was reported to be a more stable and active catalytic surface. In brief, the FeCoNiPdWOOH, FeCoNiPdOOH, FeCoNiWPOOH, FeCoPdWOOH, FeNiPdWOOH, and CoNiPdWOOH (built on the FeOOH model in which Co/Ni/Pd/W atoms were doped on the surface to substitute for Fe atoms) were chosen as the local configurations (Figs. S19-25). As for the theoretical simulations for ORR, the initial HEPs (mainly composed of W-P and Pd-P) hydride with MOH (enrichment of

Fe/Co/Ni, while Pd and W atoms alternatively doped on the subsurface) with (100) terminated surface were constructed (Fig. S49). Notice that this is a simplified approach as the modeling of the exact reconstructed HEP structure is largely hindered by its complexity, the lack of precise tools to determine it, and its probably dynamic evolution during the oxygen redox reactions.

For all the models, a 20 Å vacuum space was set on the z-axis to guarantee full relaxation. The free energy (ΔG) calculations of each elementary step were based on the standard hydrogen electrode model.[13] The reaction free energy change can be obtained with the equation below:

$$\Delta G=\Delta E + \Delta EZPE-T\Delta S \quad (1)$$

where ΔE is the total energy difference before and after intermediate adsorption, ΔEZPE and ΔS are the differences of zero-point energy and entropy, respectively.

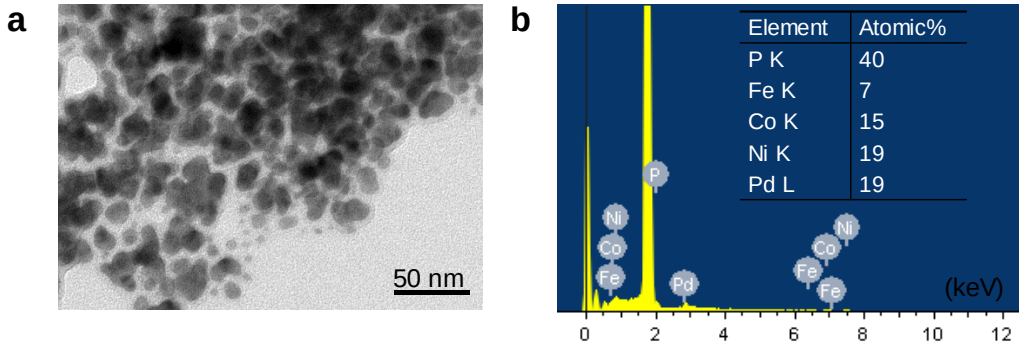

Fig. S1. (a) TEM image, and (b) EDS spectra. The inset shows the elemental composition of the FeCoNiPdP.

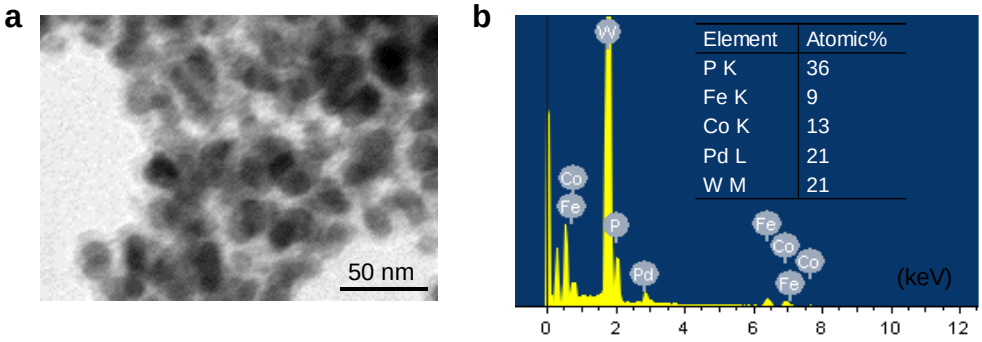

Fig. S2. (a) TEM image, and (b) EDS spectra. The inset shows the elemental composition of the FeCoPdWP.

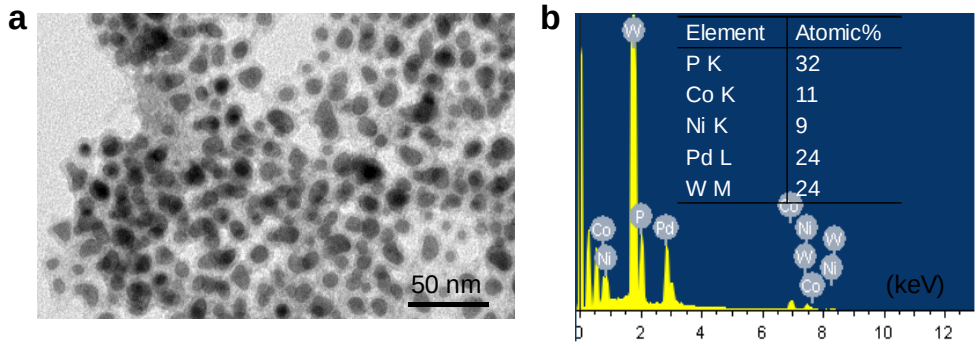

Fig. S3. (a) TEM image, and (b) EDS spectra. The inset shows the elemental composition of the CoNiPdWP.

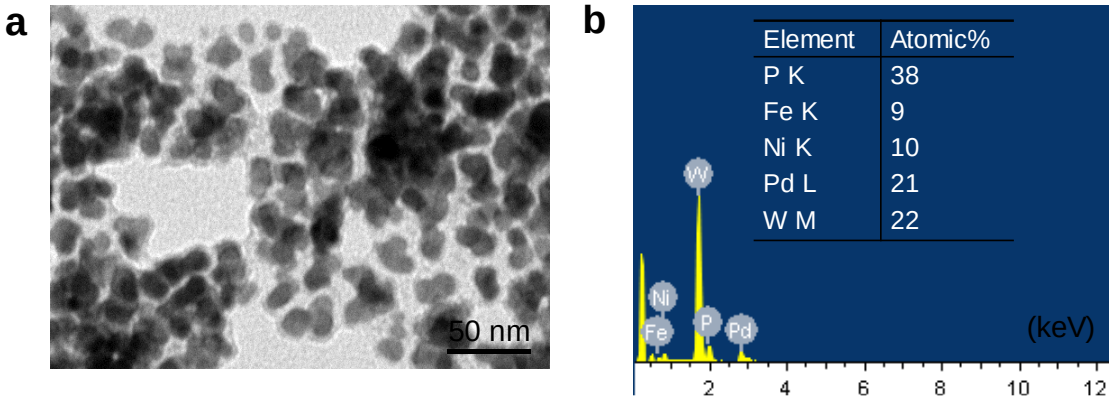

Fig. S4. (a) TEM image, and (b) EDS spectra. The inset shows the elemental composition of the FeNiPdWP.

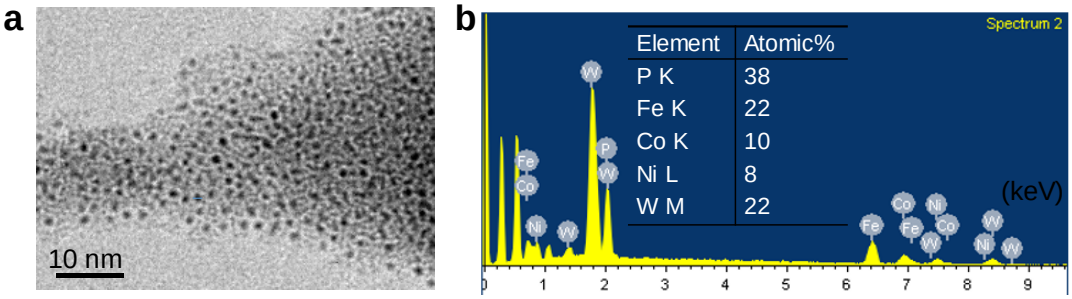

Fig. S5. (a) TEM image, and (b) EDS spectra. The inset shows the elemental composition of the FeCoNiWP.

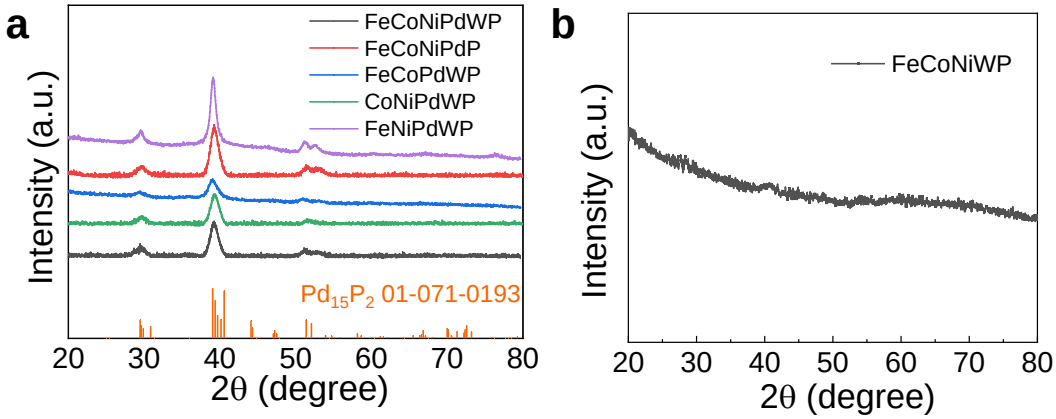

Fig. S6. XRD pattern of (a) FeCoNiPdWP, FeCoNiPdP, FeCoPdWP, CoNiPdWP, and FeNiPdWP, and (b) FeCoNiWP.

Fig. S1-S5 show the transmission electron microscopy (TEM) images, energy-dispersive X-ray spectroscopy (EDS) spectra, and the EDS elemental composition of FeCoNiPdP, FeCoPdWP, CoNiPdWP, FeNiPdWP, and FeCoNiWP. TEM images show the average particle size of the quaternary metal phosphides containing Pd to be ca. 10-20 nm while the Pd-free FeCoNiWP nanoparticles show a significantly smaller average size of ~2 nm. This different particle size can be related to the role played by Pd in the formation of the initial nuclei where the different elements are subsequently incorporated. X-ray diffraction (XRD) patterns of FeCoNiPdP, FeCoPdWP, CoNiPdWP, and FeNiPdWP show the Pd-based materials to present a good crystallinity (Fig. S6a). The main peaks around 30°, 40°, 51°, and 52° match the $Pd_{15}P_2$ rhombohedral phase (JCPDS 01-071-0193). This is consistent with Pd-P forming the initial crystal seed and the other metals gradually incorporating during the synthesis process. The less intense XRD peaks within the $Pd_{15}P_2$ reference pattern are not observed due to the lattice distortions associated with the replacement of Pd with the different metals (Fe, Co, Ni, W). In contrast, XRD analysis shows the Pd-free sample, FeCoNiWP, to be mostly amorphous (Fig. S6b), further confirming the essential role played by Pd in the formation of the nanocrystals.

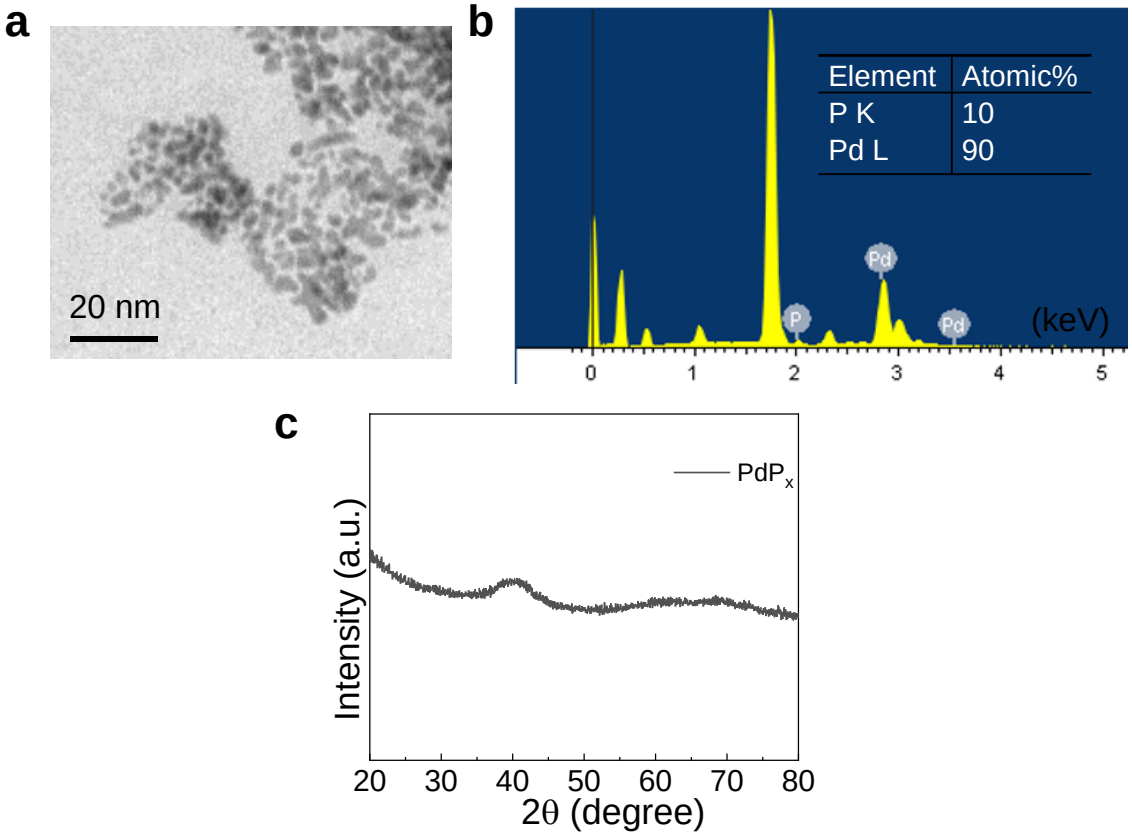

Fig. S7. (a) TEM image, (b) EDS spectra. The inset shows the elemental composition. (c) XRD pattern of the PdP_x.

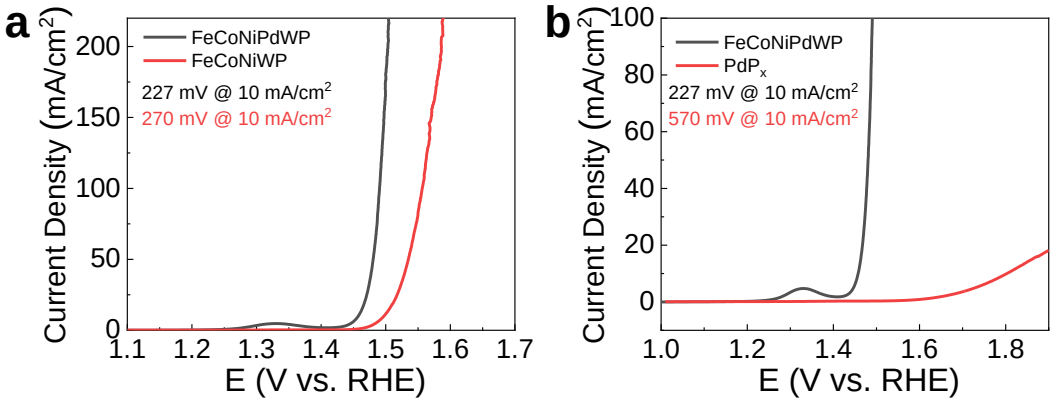

Fig. S8. (a) OER LSV curves of FeCoNiPdWP and FeCoNiWP. (b) OER LSV curves of FeCoNiPdWP and PdP_x.

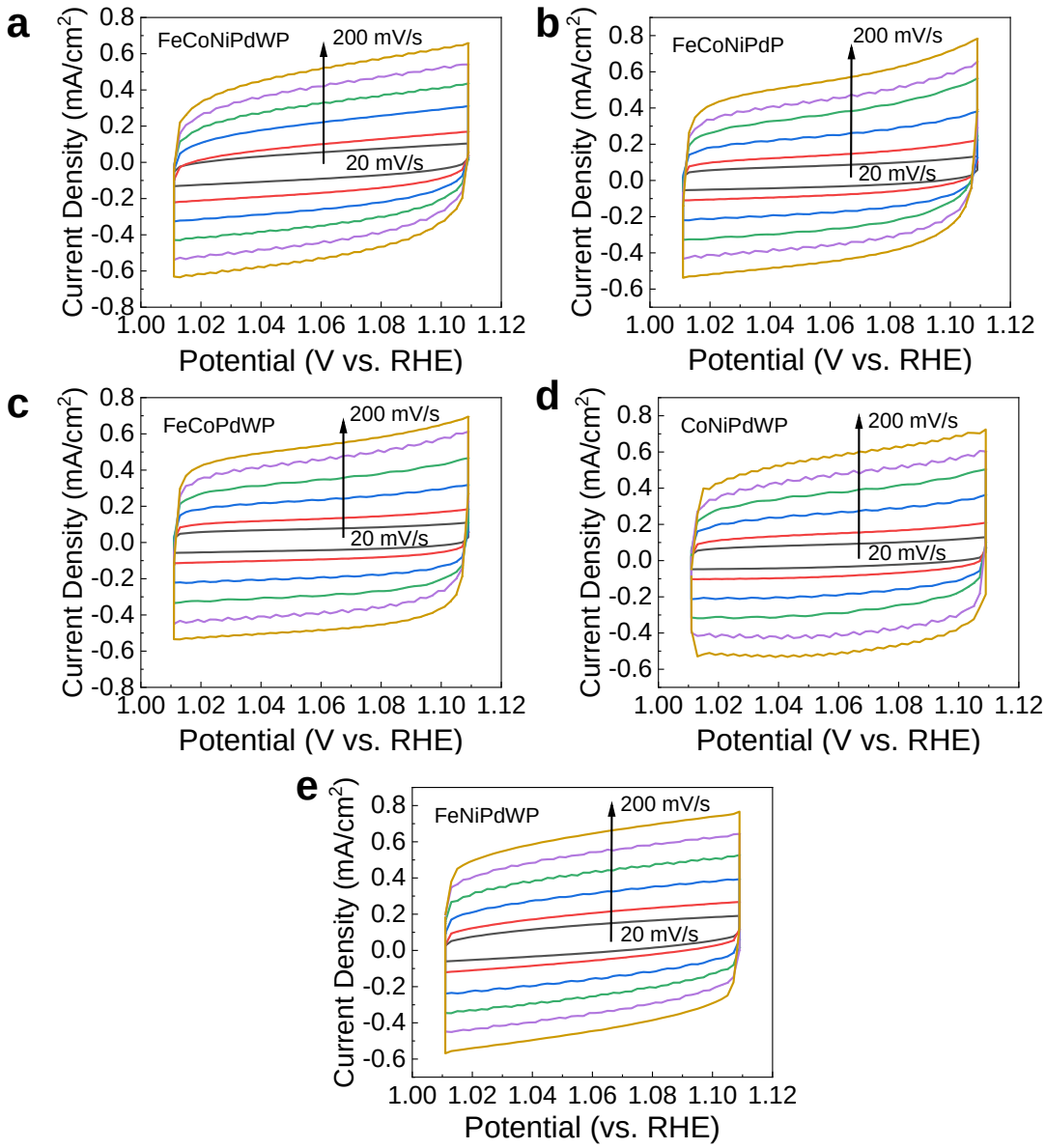

Fig. S9. CV curves of (a) FeCoNiPdWP, (b) FeCoNiPdP, (c) FeCoPdWP, (d) CoNiPdWP, and (e) FeNiPdWP at different scan rates from 20 to 200 mV/s for fitting and calculating the C_{dl} values in Fig. 2d.

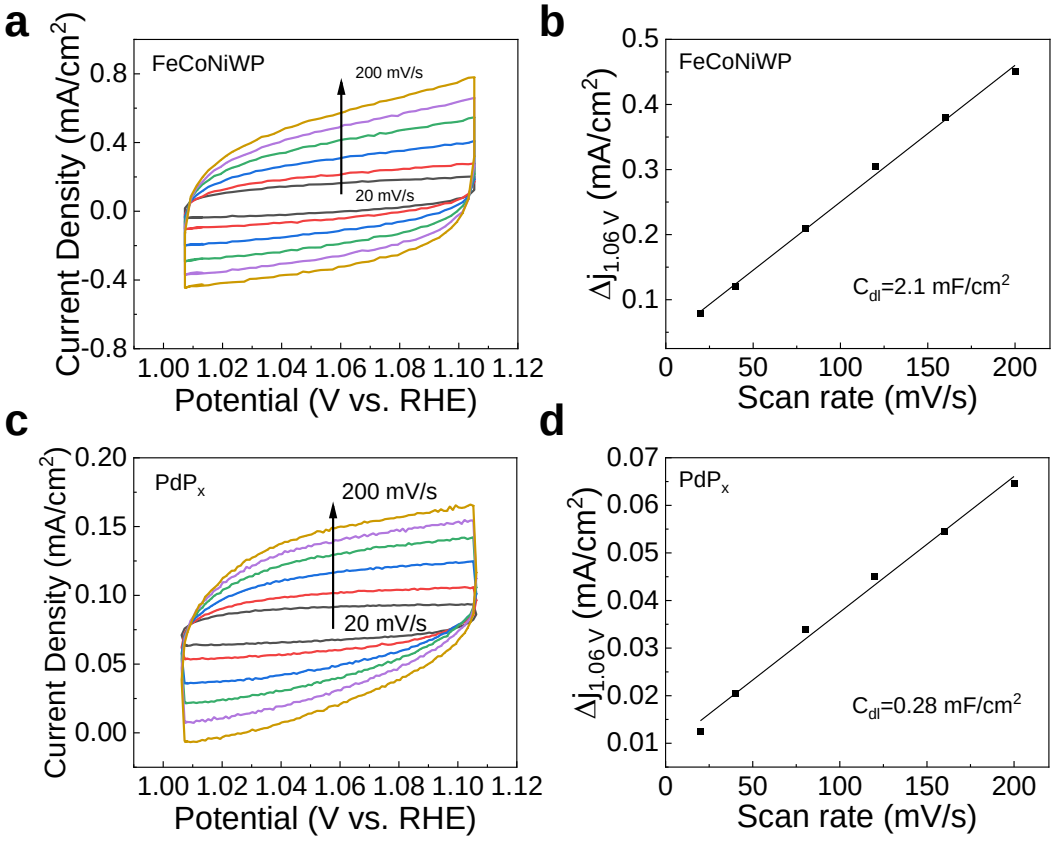

Fig. S10. CV curves of (a) FeCoNiWP and (c) PdP_x at different scan rates from 20 to 200 mV/s. C_{dl} values of (b) FeCoNiWP and (d) PdP_x.

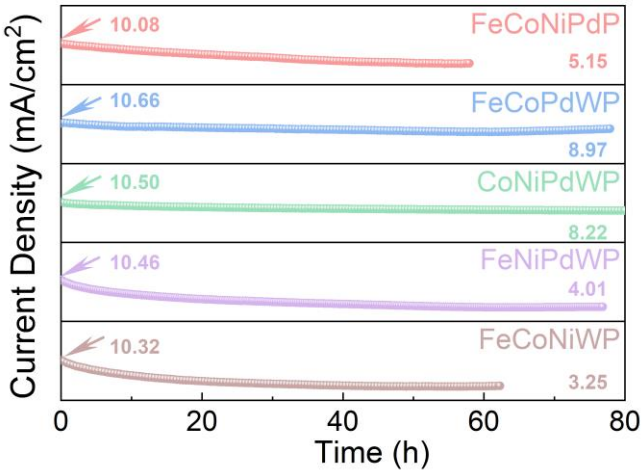

Fig. S11. OER stability test of FeCoNiPdP, FeCoPdWP, CoNiPdWP, FeNiPdWP, and FeCoNiWP with CA technique.

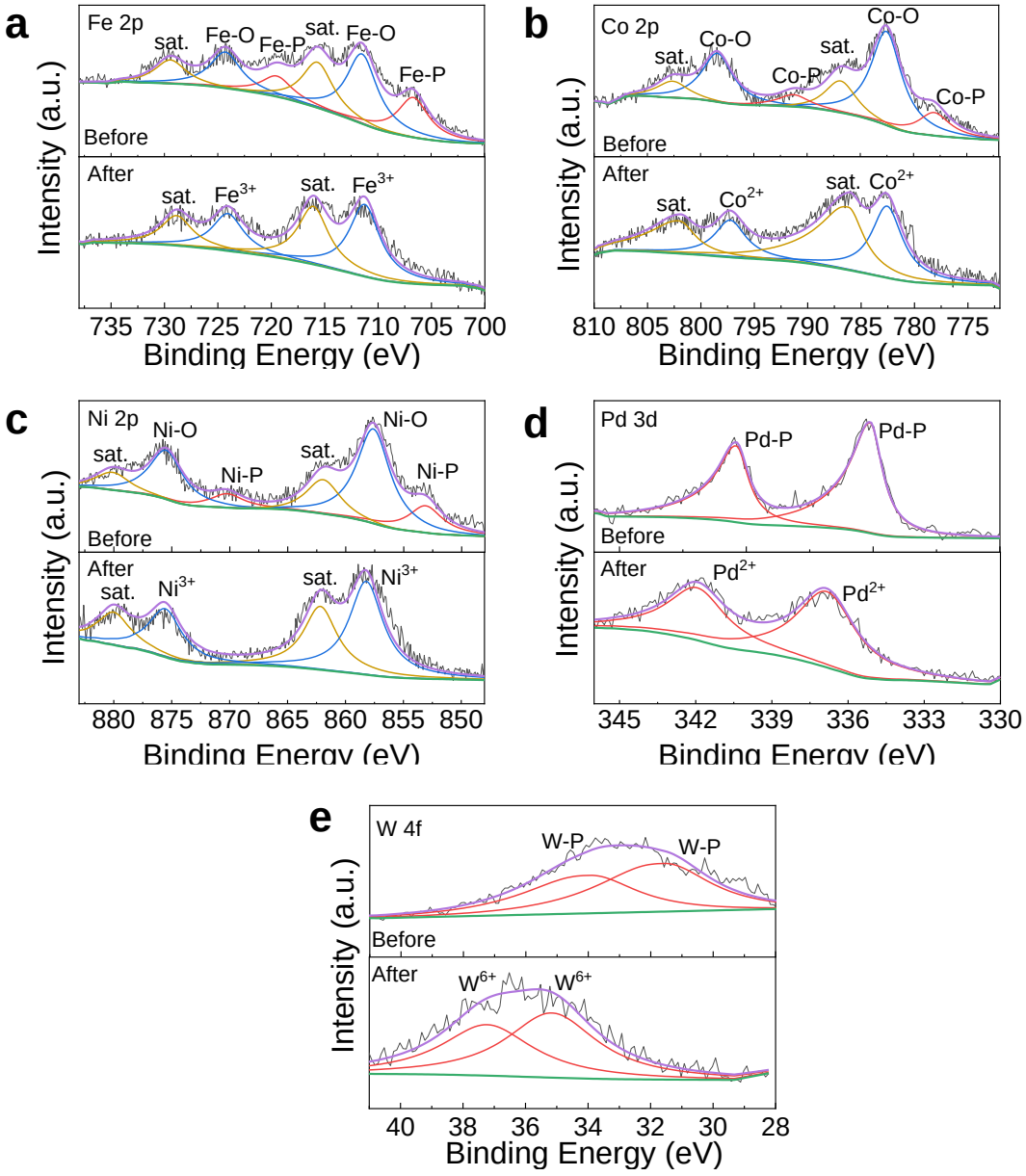

Fig. S12. High-resolution (a) Fe 2p, (b) Co 2p, (c) Ni 2p, (d) Pd 3d, and (e) W 4f XPS spectra of FeCoNiPdWP before (upward) and after (downward) OER stability test.

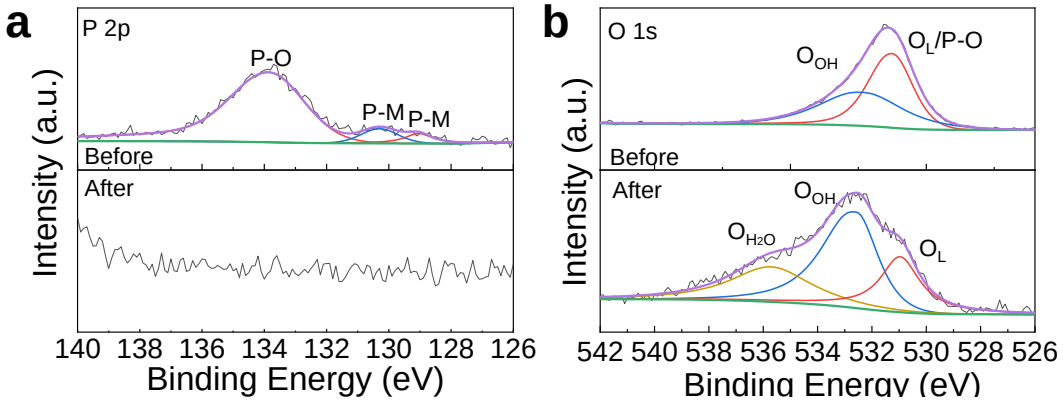

Fig. S13. High-resolution (a) P 2p, and (b) O 1s XPS spectra of FeCoNiPdWP before (upward) and after (downward) OER stability test.

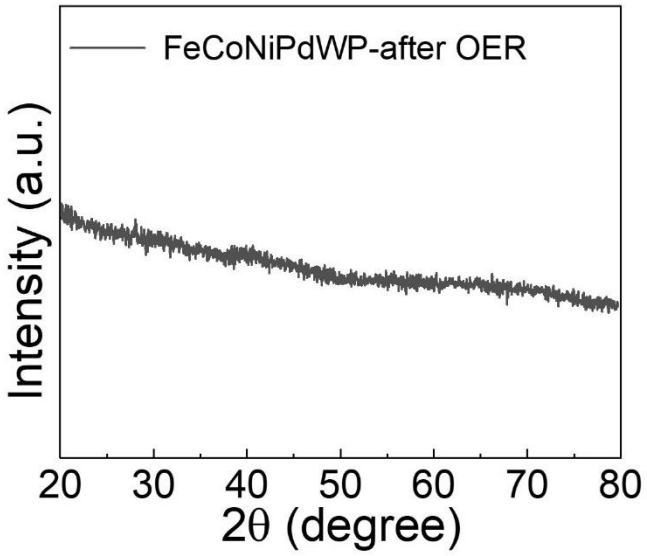

Fig. S14. XRD pattern of FeCoNiPdWP after OER stability test.

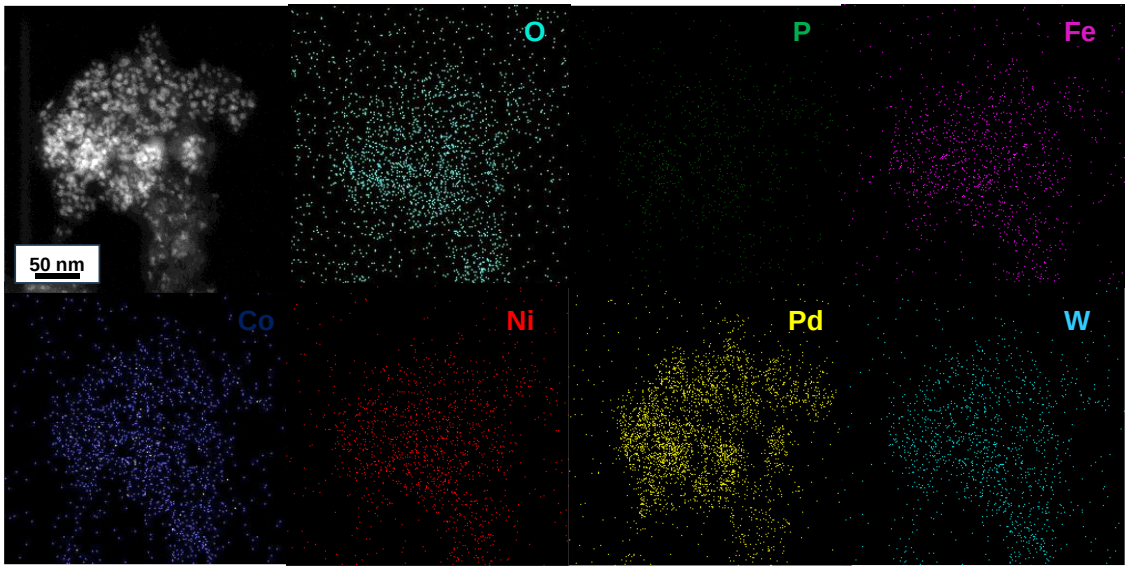

Fig. S15. HAADF STEM micrograph and EDS compositional maps for each element of FeCoNiPdWP after OER stability test.

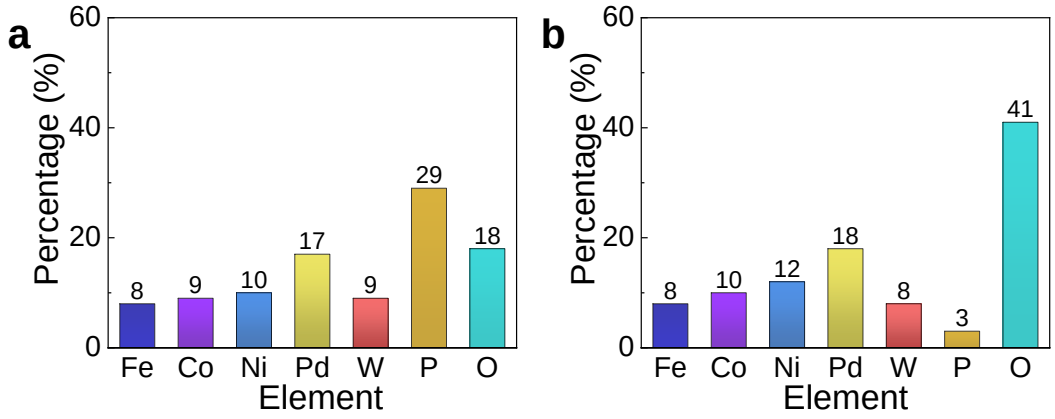

Fig. S16. Elemental composition from EDS spectra of FeCoNiPdWP HEPs (a) before the OER test, and (b) after the OER test.

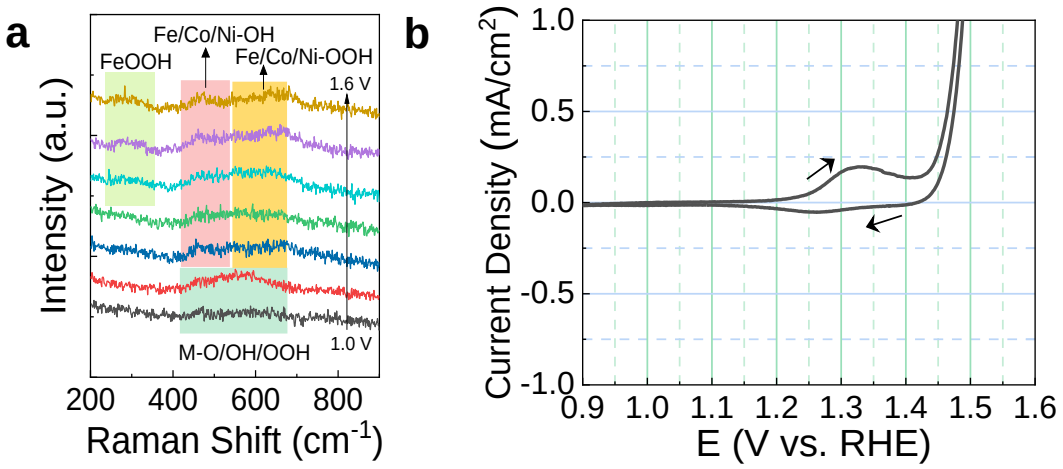

Fig. S17. (a) *In situ* Raman spectra taken at Raman shift range of 200-900 cm^{-1}. The vertical arrows mark the two most prominent vibrations and their assignment to vibrations of the Fe/Co/Ni-OH and Fe/Co/Ni-OOH. The Raman spectra was taken at a potential that is shown as vertical line in the CV curves. (b) CV curves with the scan rate of 5 mV/s in 1 M KOH of FeCoNiPdWP. The black arrows mark the scan direction.

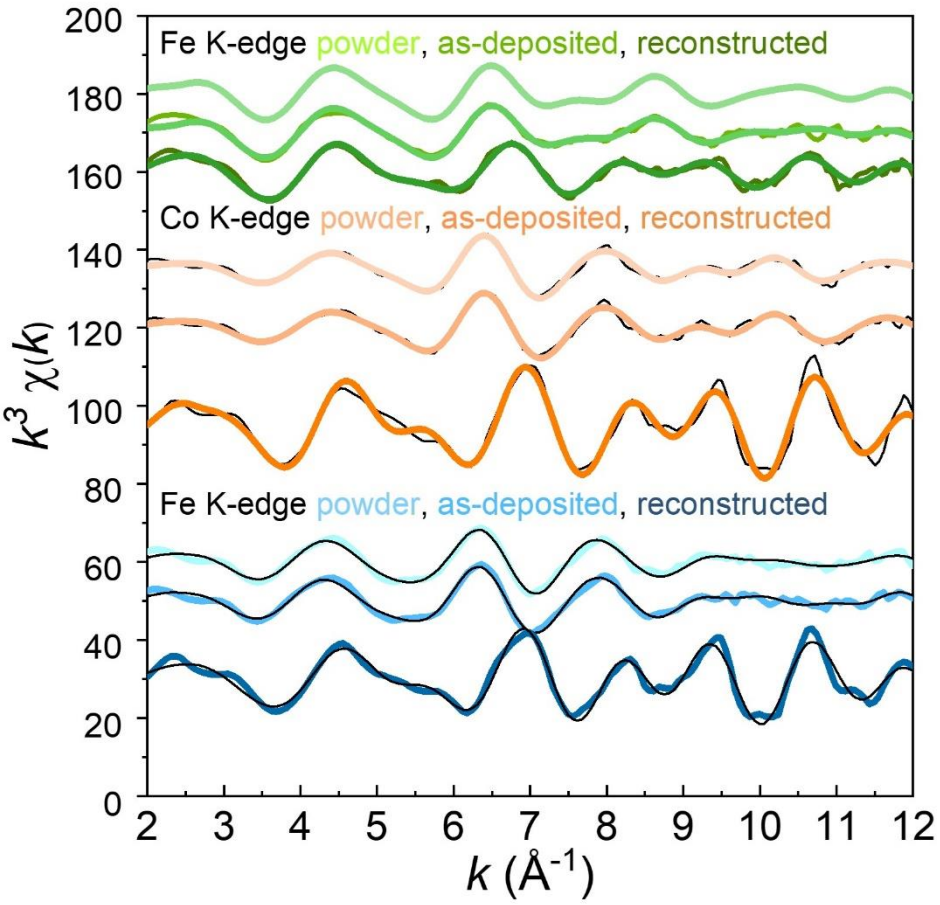

Fig. S18. k^3-weighted EXAFS spectra of the Fe, Co, Ni K-edge of the as-prepared powder, the as-deposited film, and reconstructured *in situ* freeze-quenched at 1.53 V vs. RHE after 2 h OER operation. Simulations are shown as black lines. The Fourier-transformed EXAFS data is shown in Fig. 3g, 3h, and 3i and the data used for the simulation is shown in Table 4.

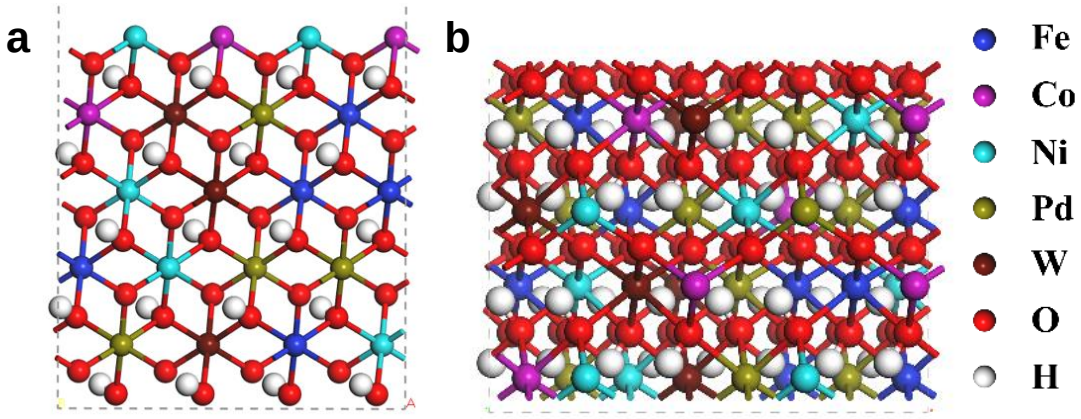

Fig. S19. Optimal theoretical model of FeCoNiPdWOOH. (a) side view, (b) top view.

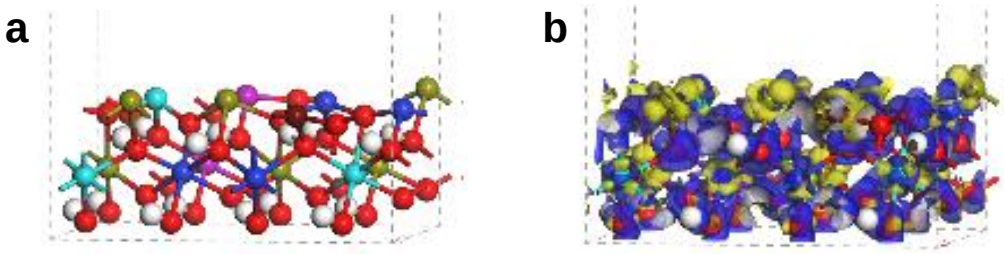

Fig. S20. (a) Optimal theoretical model of FeCoNiPdWOOH and (b) charge density difference of FeCoNiPdWOOH surfaces. Blue and yellow contours represent electron accumulation and depletion.

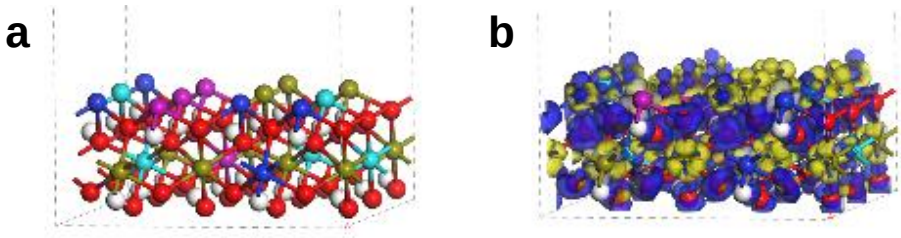

Fig. S21. (a) Optimal theoretical model of FeCoNiPdOOH and (b) charge density difference of FeCoNiPdOOH surfaces. Blue and yellow contours represent electron accumulation and depletion.

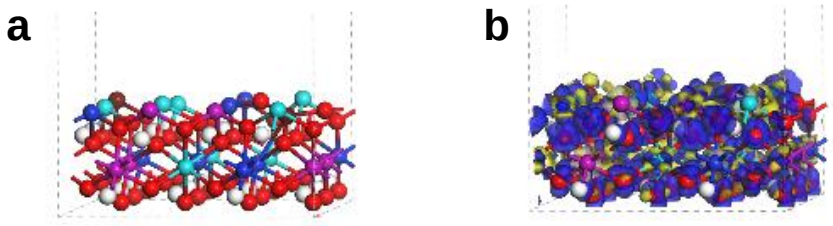

Fig. S22. (a) Optimal theoretical model of FeCoNiWOOH and (b) charge density difference of FeCoNiWOOH surfaces. Blue and yellow contours represent electron accumulation and depletion.

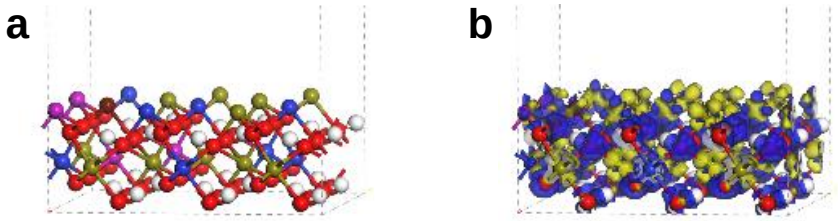

Fig. S23. (a) Optimal theoretical model of FeCoPdWOOH and (b) charge density difference of FeCoPdWOOH surfaces. Blue and yellow contours represent electron accumulation and depletion.

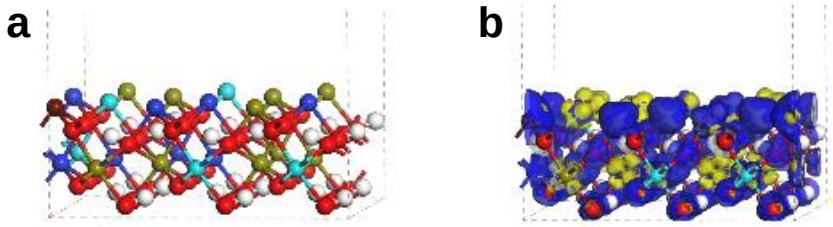

Fig. S24. (a) Optimal theoretical model of FeNiPdWOOH and (b) charge density difference of FeNiPdWOOH surfaces. Blue and yellow contours represent electron accumulation and depletion.

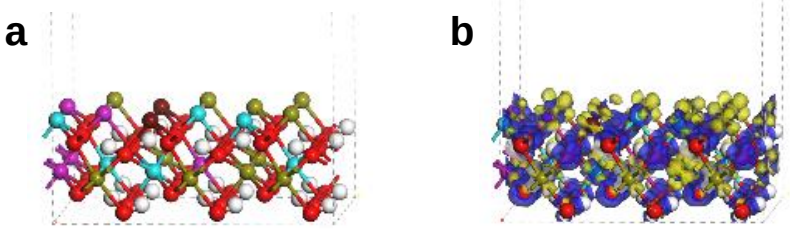

Fig. S25. (a) Optimal theoretical model of CoNiPdWOOH and (b) charge density difference of CoNiPdWOOH surfaces. Blue and yellow contours represent electron accumulation and depletion.

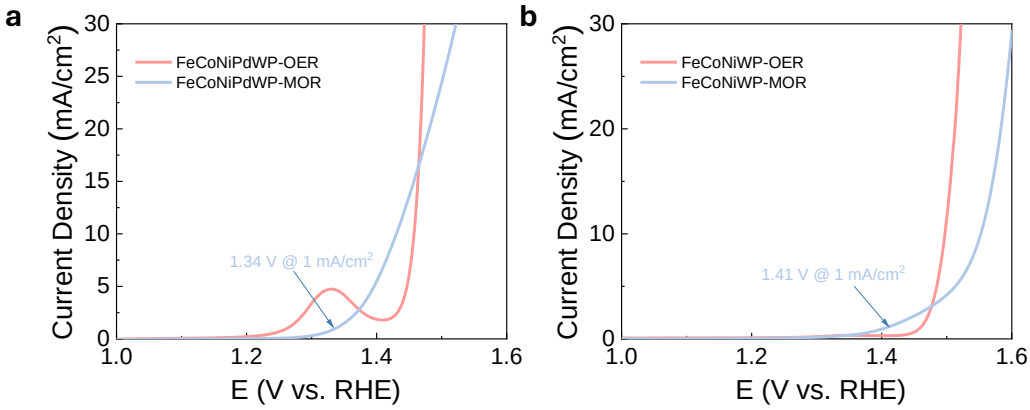

Fig. S26. The OER and methanol oxidation reaction (MOR) LSV curves of (a) FeCoNiPdWP and (b) FeCoNiWP.

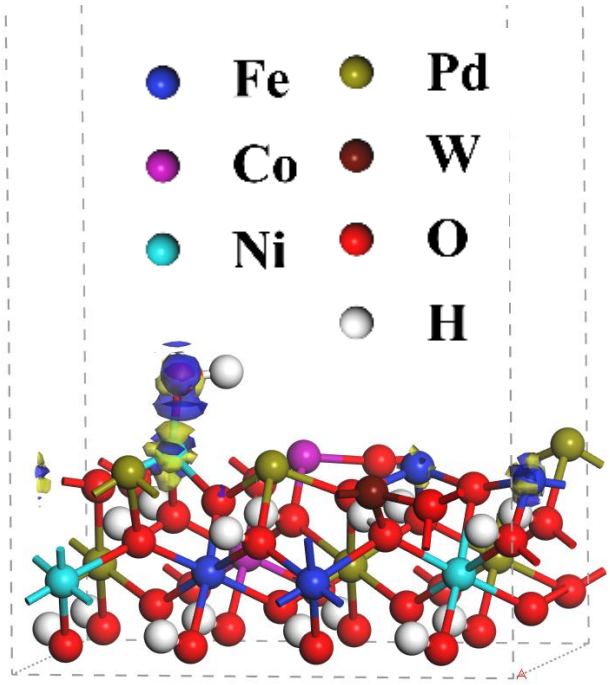

Fig. S27. CDD of OH adsorption on Ni sites over the FeCoNiPdWOOH surface. Blue and yellow contours represent electron accumulation and depletion, where the isosurface is set to 0.05 e Å^{-3}.

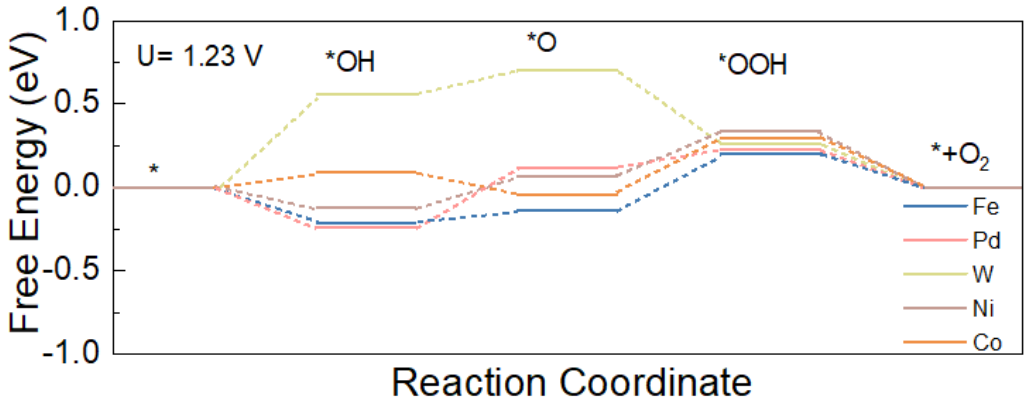

Fig. S28. Standard free energy diagram of the OER process at 1.23 V of FeCoNiPdWOOH for various active sites.

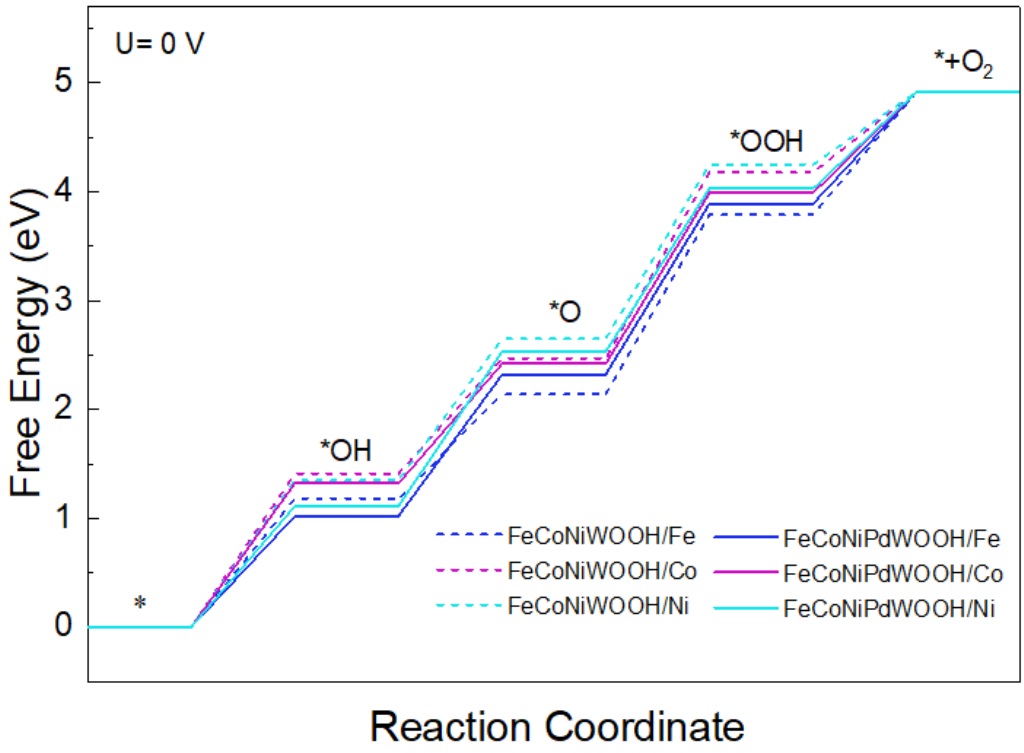

Fig. S29. Standard free energy diagram of the OER process at 0 V of various active sites on the different surface-reconstructed samples.

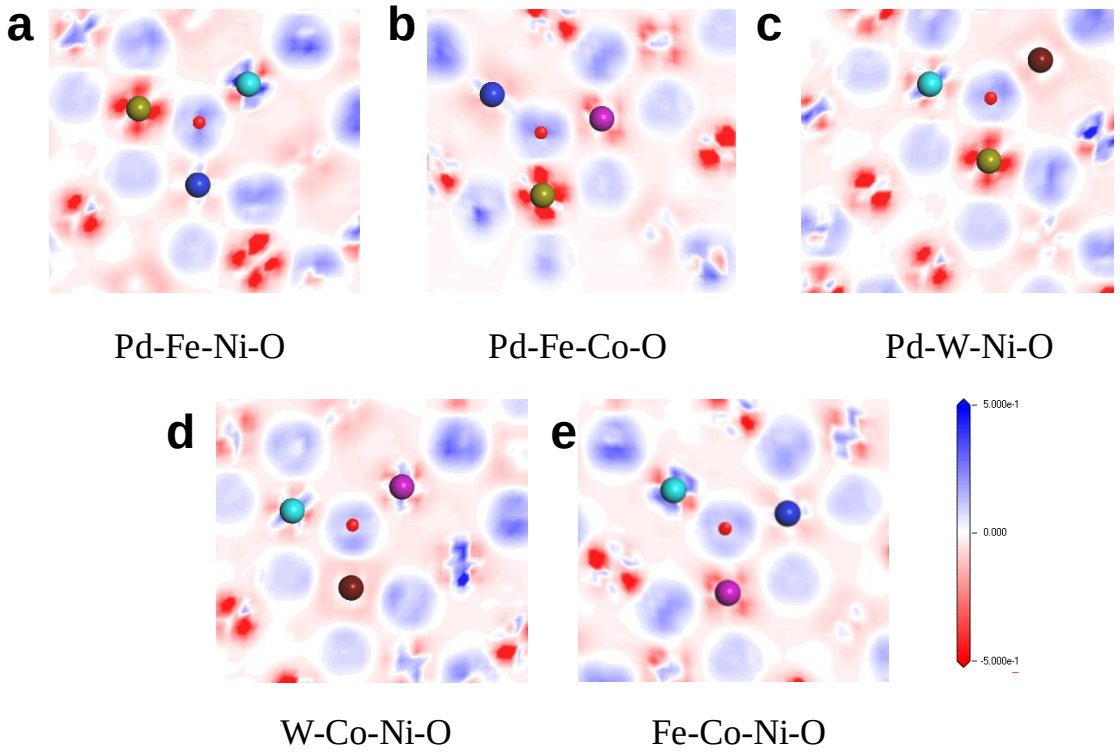

Fig. S30. 2D CDD of various M-O configurations in FeCoNiPdWOOH. (a) Pd-Fe-Ni-O, (b) Pd-Fe-Co-O, (c) Pd-W-Ni-O, (d) W-Co-Ni-O, and (e) Fe-Co-Ni-O. Blue and red contours represent electron accumulation and depletion.

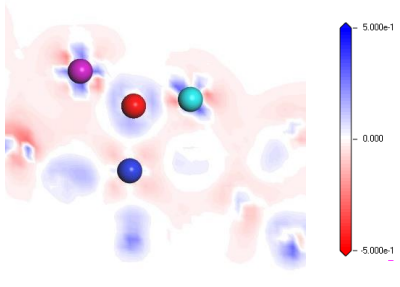

Fig. S31. 2D CDD of Fe-Co-Ni-O configurations in FeCoNiWOOH. Blue and red contours represent electron accumulation and depletion.

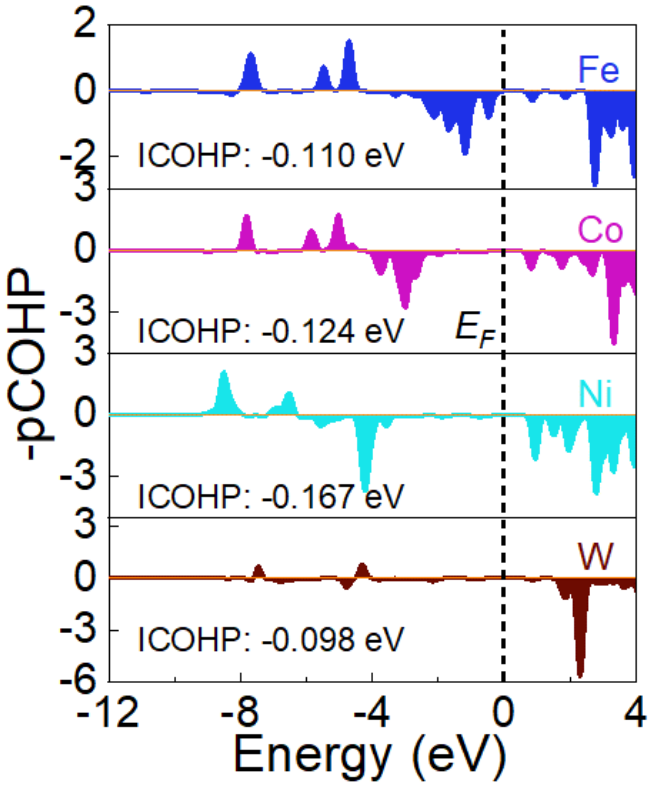

Fig. S32. The projected crystal orbital Hamilton population (pCOHP) bonding analysis of M-O interactions (M in the surface site over FeCoNiWOOH and O in adsorbed OH).

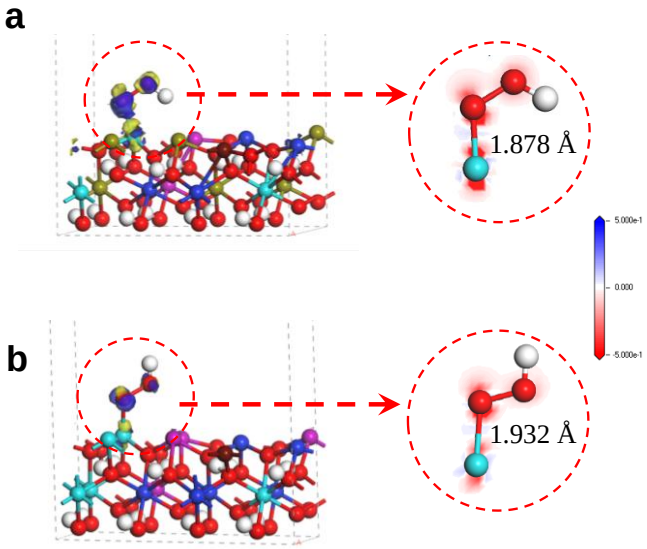

Fig. S33. Adsorption configurations and charge analysis of OOH intermediates over (a) FeCoNiPdWOOH and (b) FeCoNiWOOH (b) surfaces. Blue and yellow (in 3D mode) / red (in 2D mode) contours represent electron accumulation and depletion.

2D CDD results show that Pd-containing M-O configurations (M=metal site; O=oxygen from the reconstructed HEOOH) within FeCoNiPdWOOH display more efficient site-to-site electron transfer than the Pd-free ones (Fig. S30 and S31). The ICOHP values of the metal sites in FeCoNiPdWOOH are all larger than those of the Pd-free FeCoNiWOOH model (Fig. S32), indicating the presence of Pd to optimize the adsorption configuration. As shown in Fig. S33, the bond length of Ni-*OOH in FeCoNiPdWOOH (1.878 Å) is smaller than in FeCoNiWOOH (1.932 Å), indicating a stronger electronic interaction. The calculated CDD results suggest that *OOH adsorption on the FeCoNiPdWOOH surface resulted in a stronger local charge redistribution over the active sites than that of FeCoNiWOOH, causing more electron migration from the surface to the adsorbed *OOH species (supported by quantitative Mulliken charge analysis).

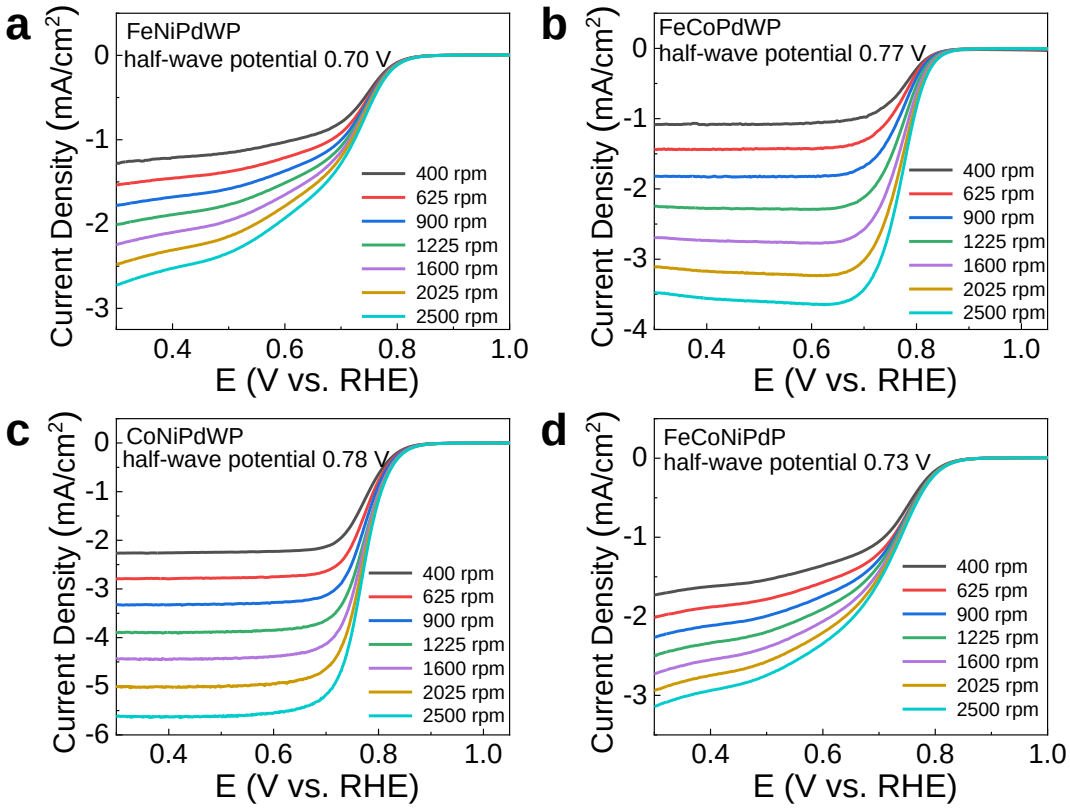

Fig. S34. LSV curves at the scan rate of 10 mV/s of ORR with different rotation speeds from 400 to 2500 rpm by using RRDE electrode with the catalysts of (a) FeNiPdWP, (b) FeCoPdWP, (c) CoNiPdWP, and (d) FeCoNiPdP.

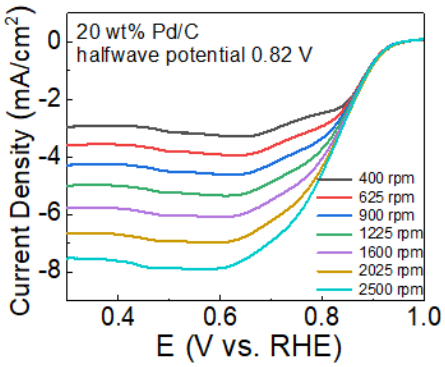

Fig. S35. LSV curves at the scan rate of 10 mV/s of ORR with different rotation speeds from 400 to 2500 rpm by using RRDE electrode with the catalysts of Pd/C.

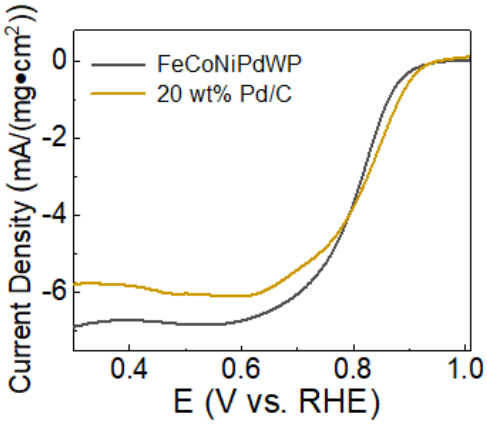

Fig. S36. LSV curves at 1600 rpm normalized to the quality of Pd for the FeCoNiPdWP and commercial Pd/C catalysts.

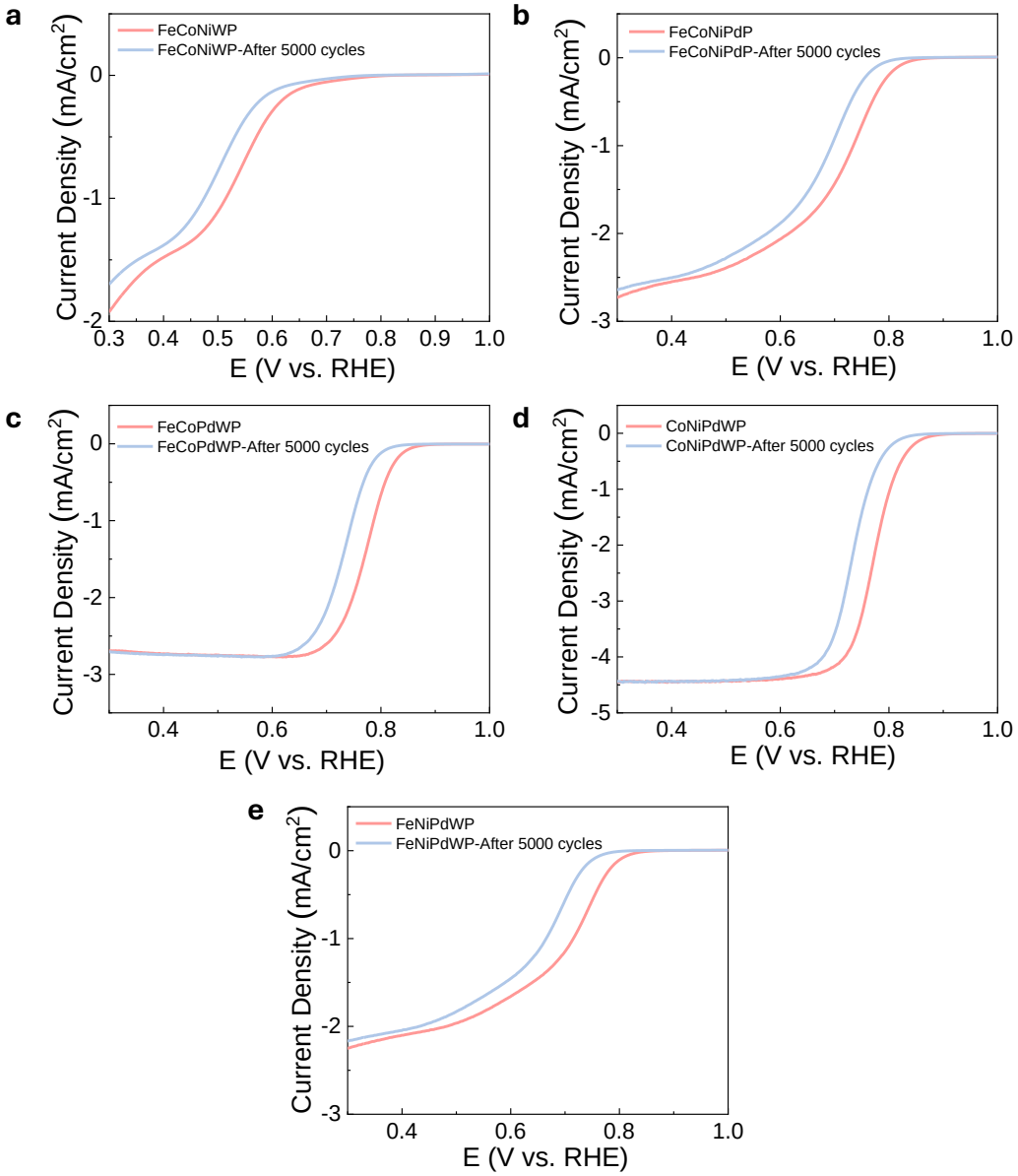

Fig. S37. ORR stability test of (a) FeCoNiWP, (b) FeCoNiPdP, (c) FeCoPdWP, (d) CoNiPdWP, and (e) FeNiPdWP with different CV cycles.

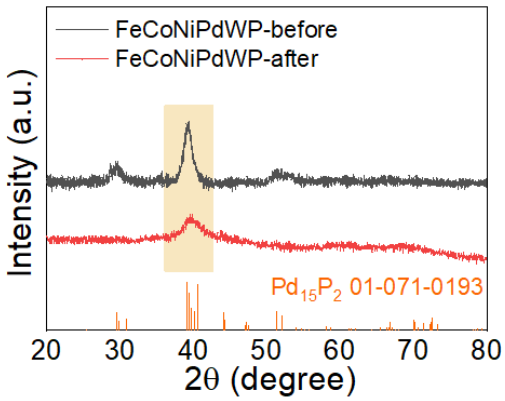

Fig. S38. XRD pattern of FeCoNiPdWP before and after ORR stability measurement.

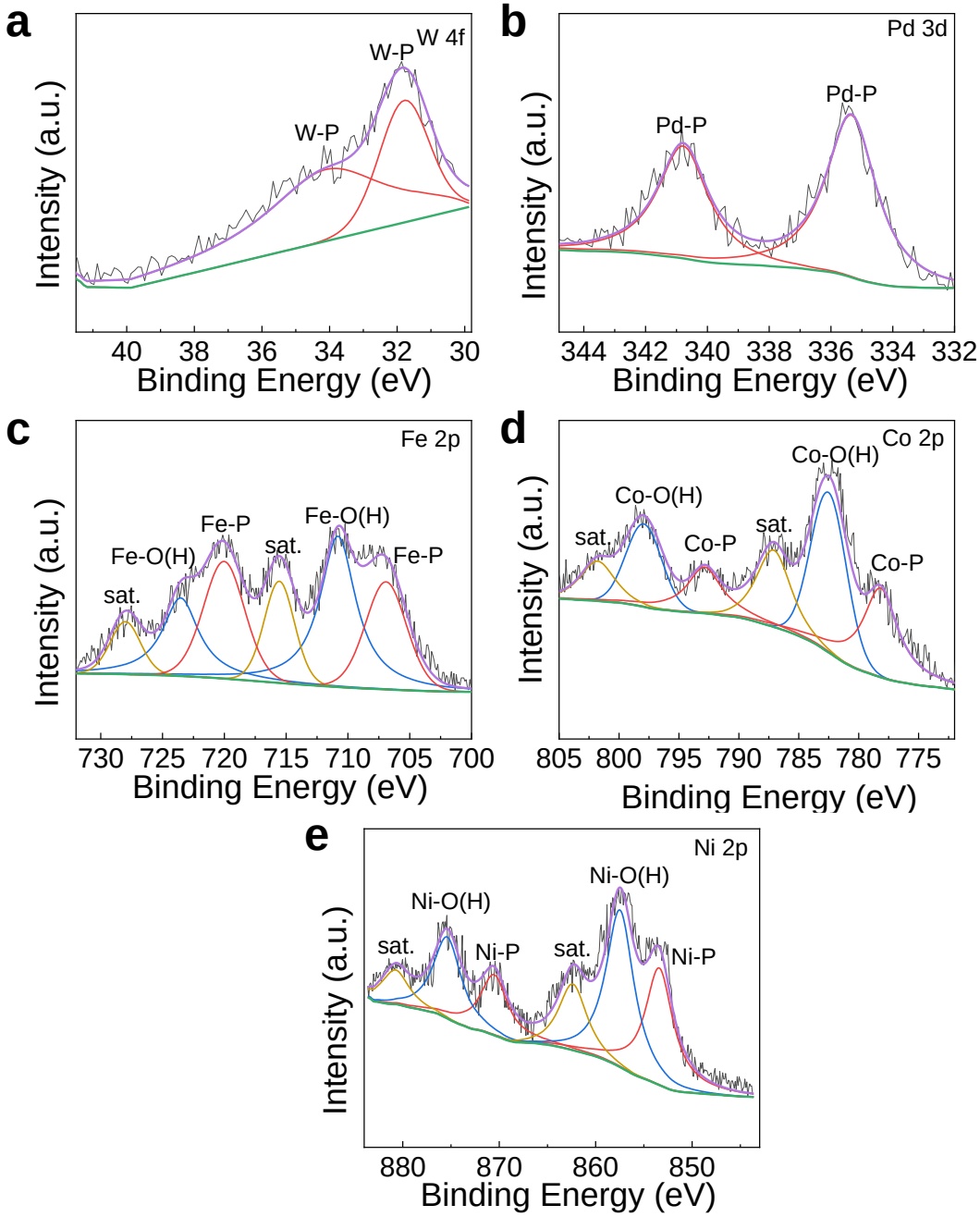

Fig. S39. High-resolution (a) W 4f, (b) Pd 3d, (c) Fe 2p, (d) Co 2p, and (e) Ni 2p XPS spectra for FeCoNiPdWP after ORR stability test.

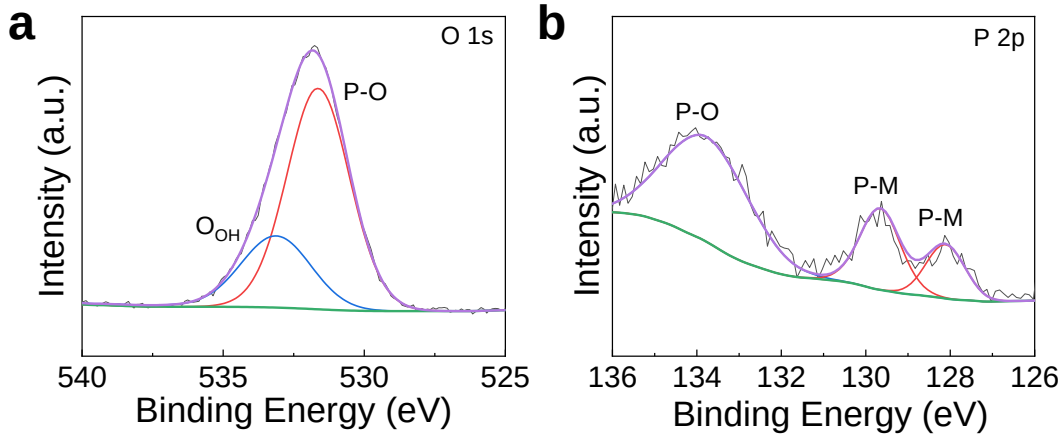

Fig. S40. High-resolution (a) O 1s, and (b) P 2p XPS spectra for FeCoNiPdWP after ORR stability test.

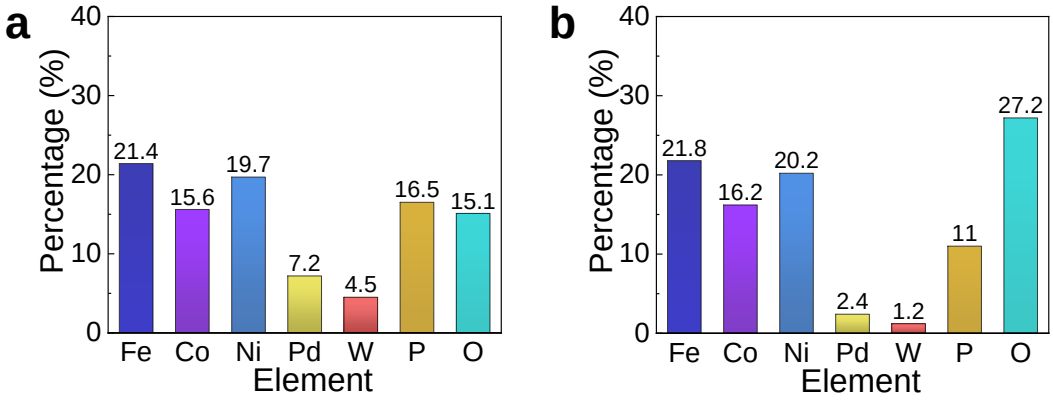

Fig. S41. Elemental composition from XPS spectra of FeCoNiPdWP HEPs surface (a) before the ORR test, and (b) after the ORR test.

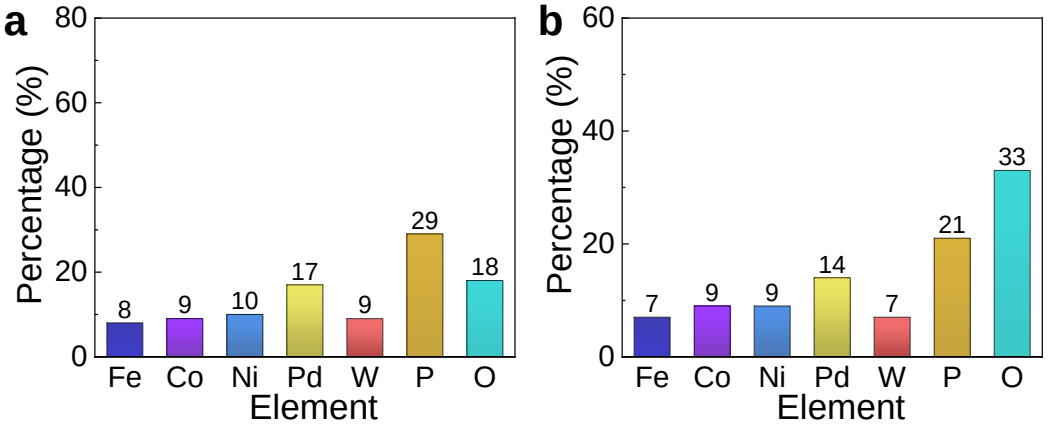

Fig. S42. Elemental composition from EDS spectra of FeCoNiPdWP HEPs (a) before the ORR test, and (b) after the ORR test.

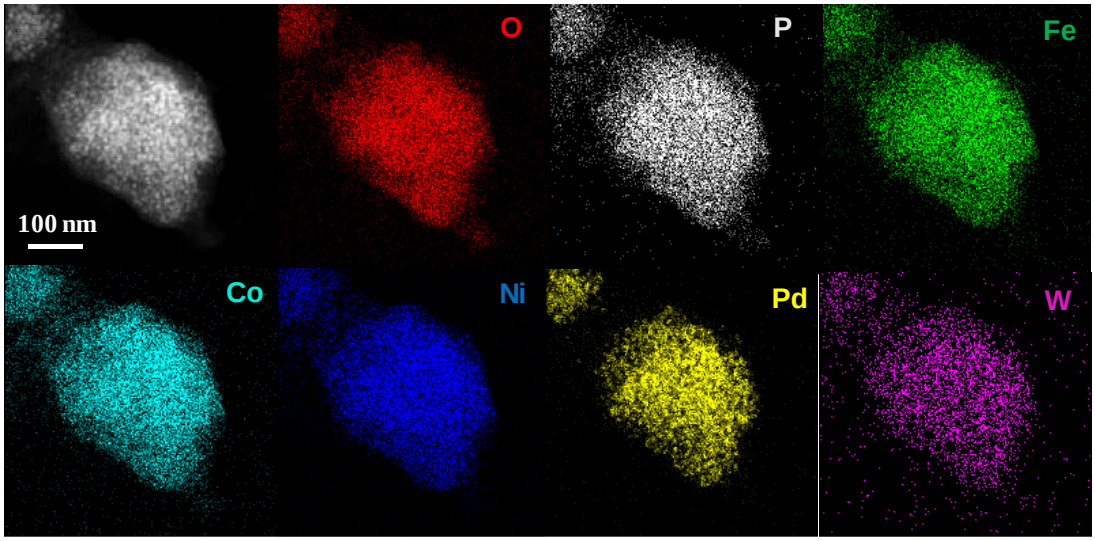

Fig. S43. HAADF STEM micrograph and EDS compositional maps for each element of FeCoNiPdWP after ORR stability test.

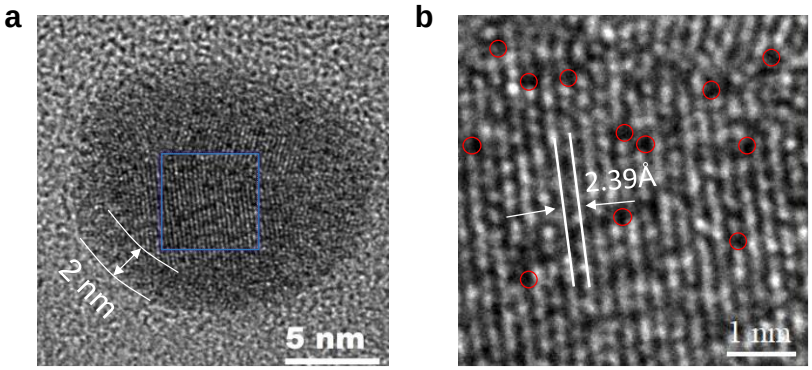

Fig. S44. (a) AC-HRTEM image of a single nanoparticle of FeCoNiPdWP after ORR stability test. (b) The magnified image of the blue square in (a). The red circles means the lattice defects after stability test. The lattice distance of 2.39 Å matches the (211) crystal plane of the rhombohedral $Pd_{15}P_2$ phase.

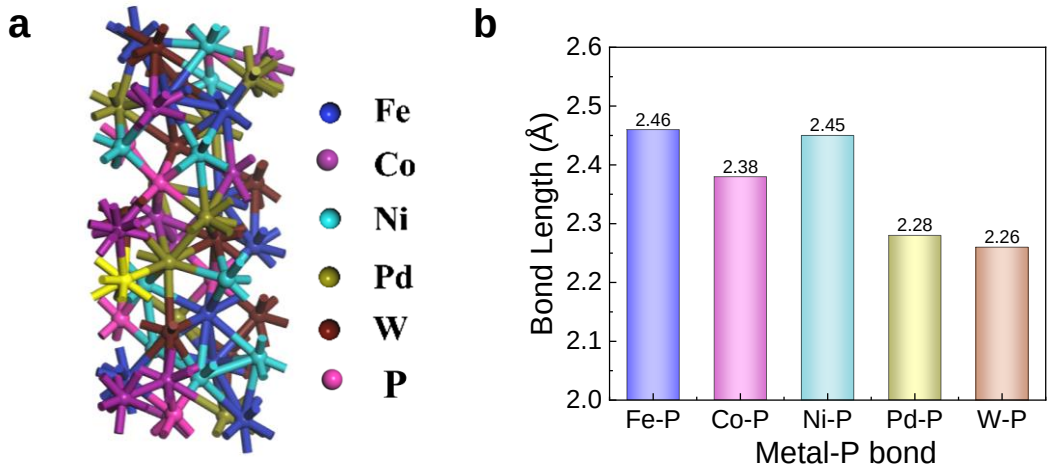

Fig. S45. (a) The optimized model of FeCoNiPdWP. (b) The metal-P bond length.

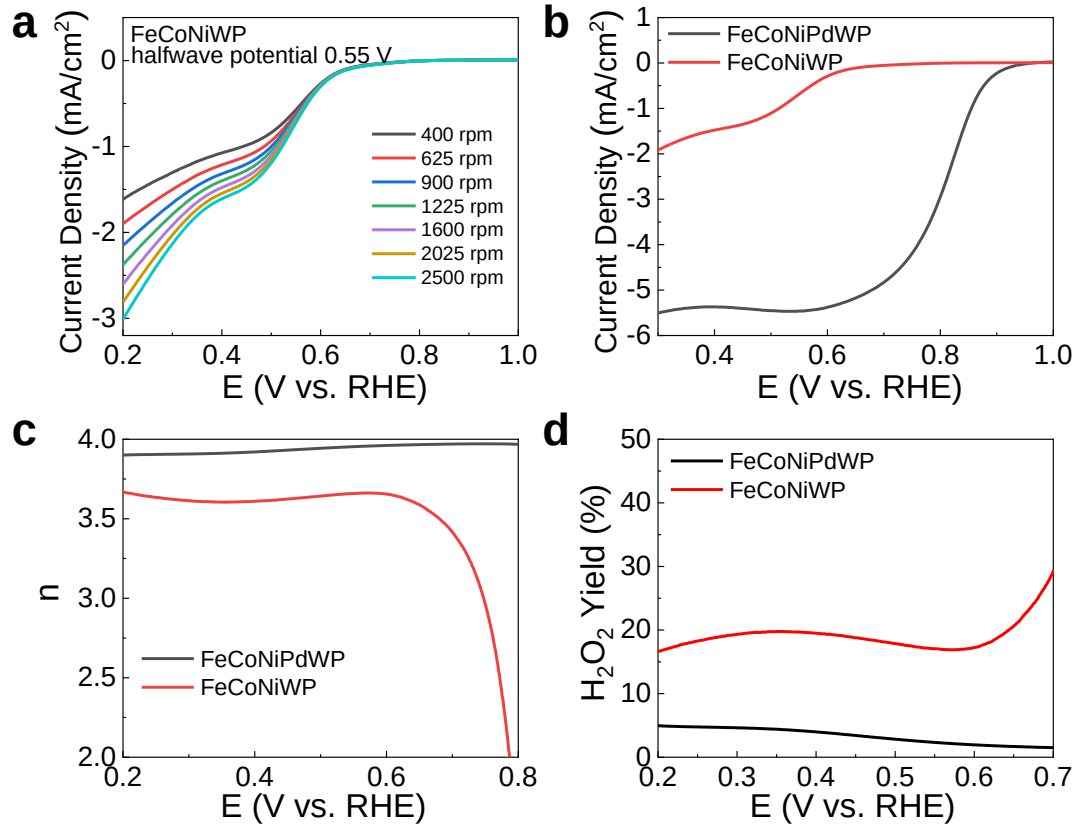

.

Fig. S46. ORR performance. (a) LSV curves of FeCoNiWP at different rotation speeds from 400-2500 rpm. (b) LSV curves at 1600 rpm for FeCoNiWP and FeCoNiPdWP. (c) The calculated n and (d) H_2O_2 yield of FeCoNiWP and FeCoNiPdWP.

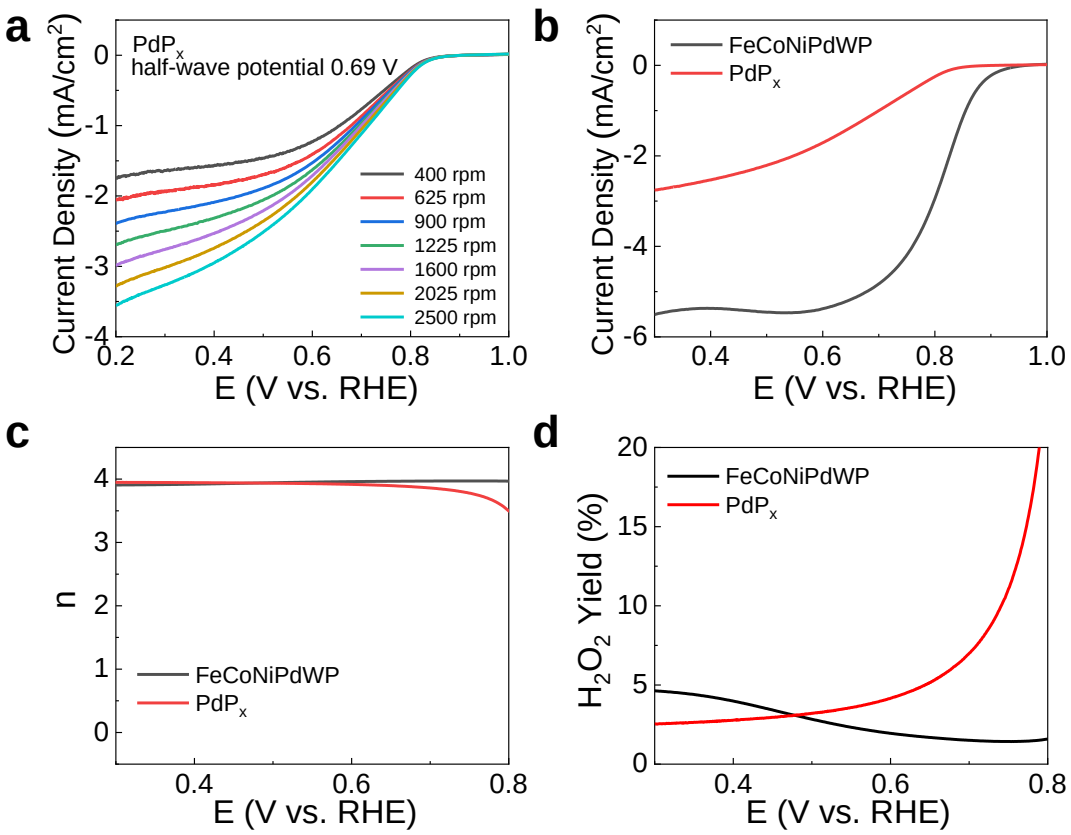

Fig. S47. ORR performance. (a) LSV curves of PdP_x at different rotation speeds from 400-2500 rpm. (b) LSV curves at 1600 rpm for PdP_x and FeCoNiPdWP. (c) The calculated n and (d) H_2O_2 yield of PdP_x and FeCoNiPdWP.

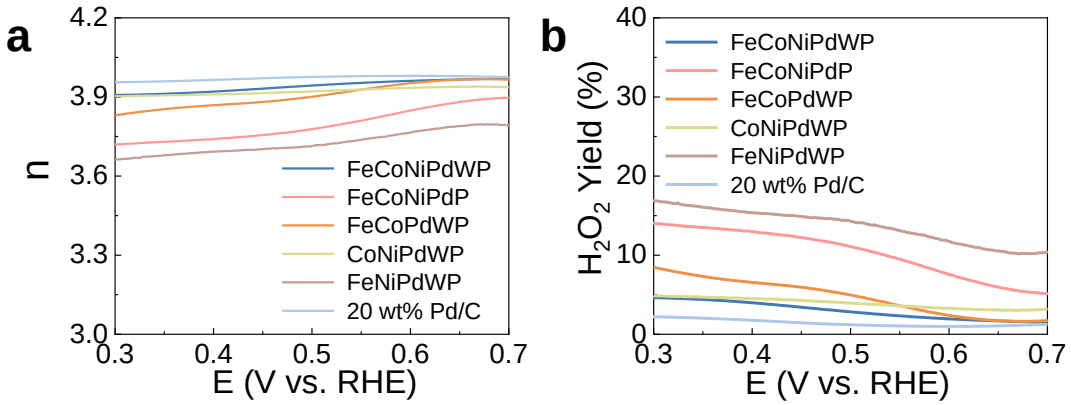

Fig. S48. (a) The calculated n and (b) H_2O_2 yield of metal phosphides and Pd/C catalysts in the potential range from 0.3-0.7 V vs. RHE.

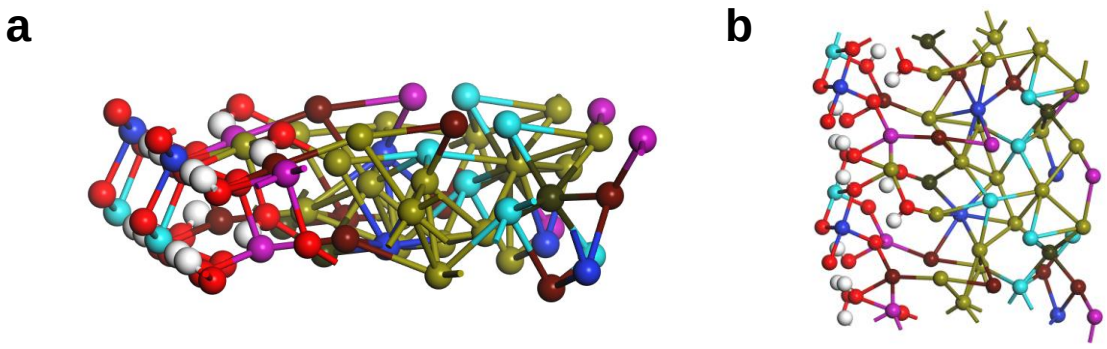

Fig. S49. The proposed FeCoNiPdWPOH models. (a) Side view and (b) top view.

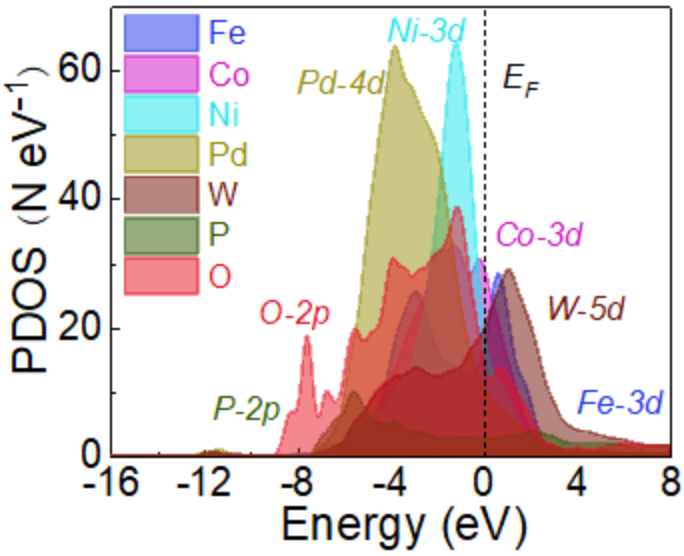

Fig. S50. PDOS of FeCoNiPdWPOH.

Pd-4d orbitals not only show a deep position as an electron reservoir but also cover the d-orbitals of other metal sites, resulting in an efficient d-d coupling effect. This guaranteed the stable valence state of the reconstructed sample during the ORR. Although the W-5d orbitals are mostly located above the E_F, there is an evident peak near the E_F that offers a high probability of losing electrons. The Ni-3d orbitals are occupied near the E_F, which supports a high electroactivity. A strong overlap between Co-3d and Ni-3d orbitals promoted efficient electron transfer between Ni and Co sites. Fe-3d orbitals exhibited an obvious e_g–t_{2g} splitting of 3.42 eV, which provides potential efficient d-d

orbital coupling between Fe and other metals. Meanwhile, the good overlap of the O-p orbitals with different metal elements implied possible p-p and p-d orbital coupling, which might further promote electron transfer efficiency.

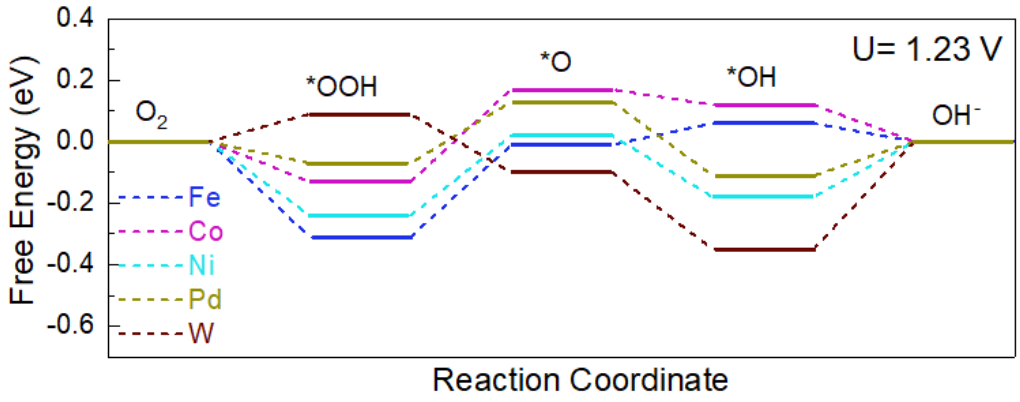

Fig. S51. Standard free energy diagram of the ORR process at 1.23 V of various active sites on the surface-reconstructed samples.

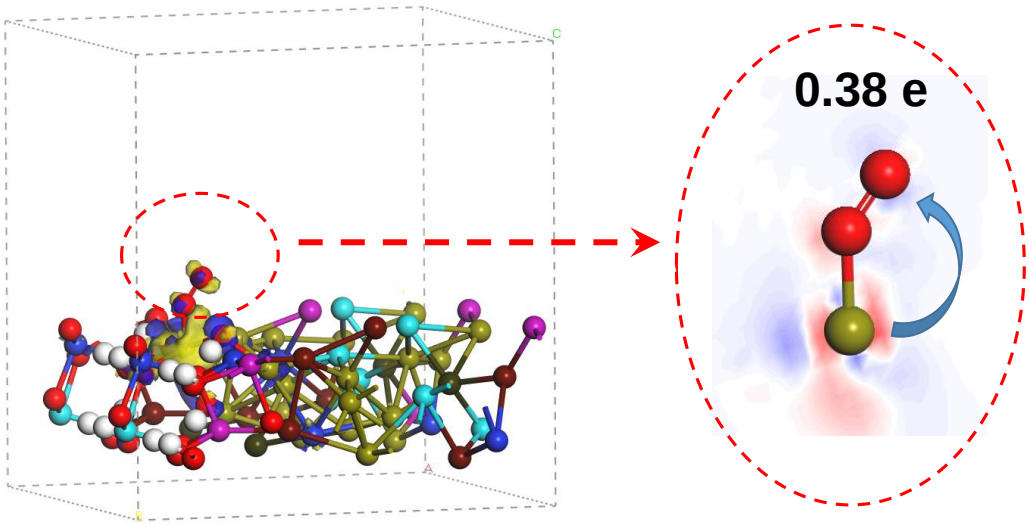

Fig. S52. CDD analysis in the constructed FeCoNiPdWPOH model containing an O_2 molecule adsorbed at the Pd site. Blue and yellow (in 3D mode) / red (in 2D mode) contours represent the regions of electron accumulation and depletion, where the isosurfaces are set to 0.05 e $Å^{-3}$.

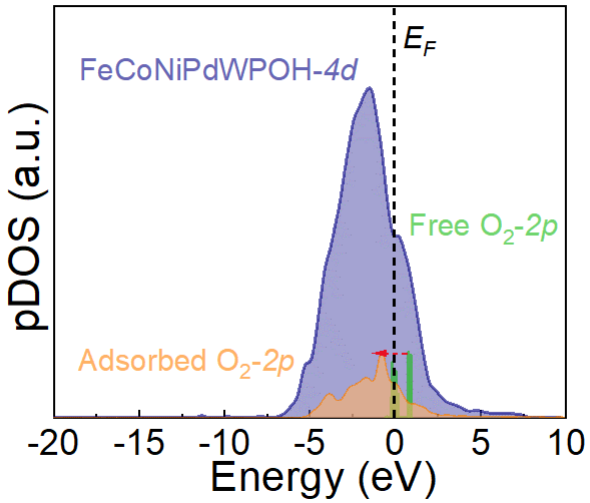

Fig. S53. PDOS for a free (green) and adsorbed (orange) O_2 molecule (2p levels) on the surface of FeCoNiPdWPOH model.

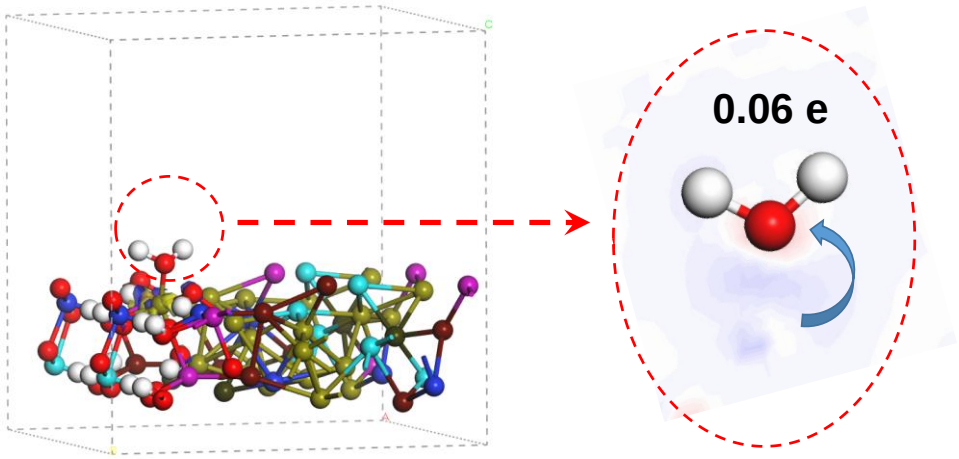

Fig. S54. CDD analysis in the constructed FeCoNiPdWPOH model containing an H_2O molecule adsorbed at the Pd site. Blue and yellow (in 3D mode) / red (in 2D mode) contours represent the regions of electron accumulation and depletion, where the isosurfaces are set to 0.05 e $Å^{-3}$.

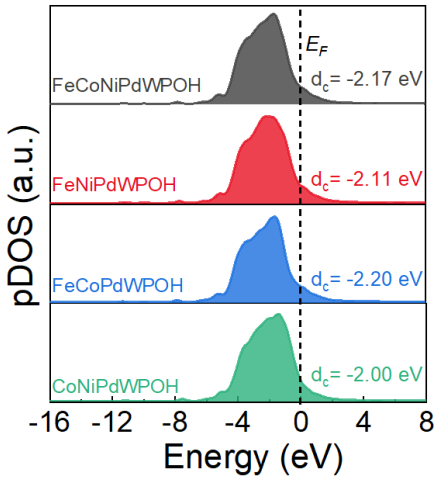

Fig. S55. The PDOS of FeCoNiPdWPOH, FeNiPdWPOH, FeCoPdWPOH, and CoNiPdWPOH models. The d-band center (d_c) energy level is also shown.

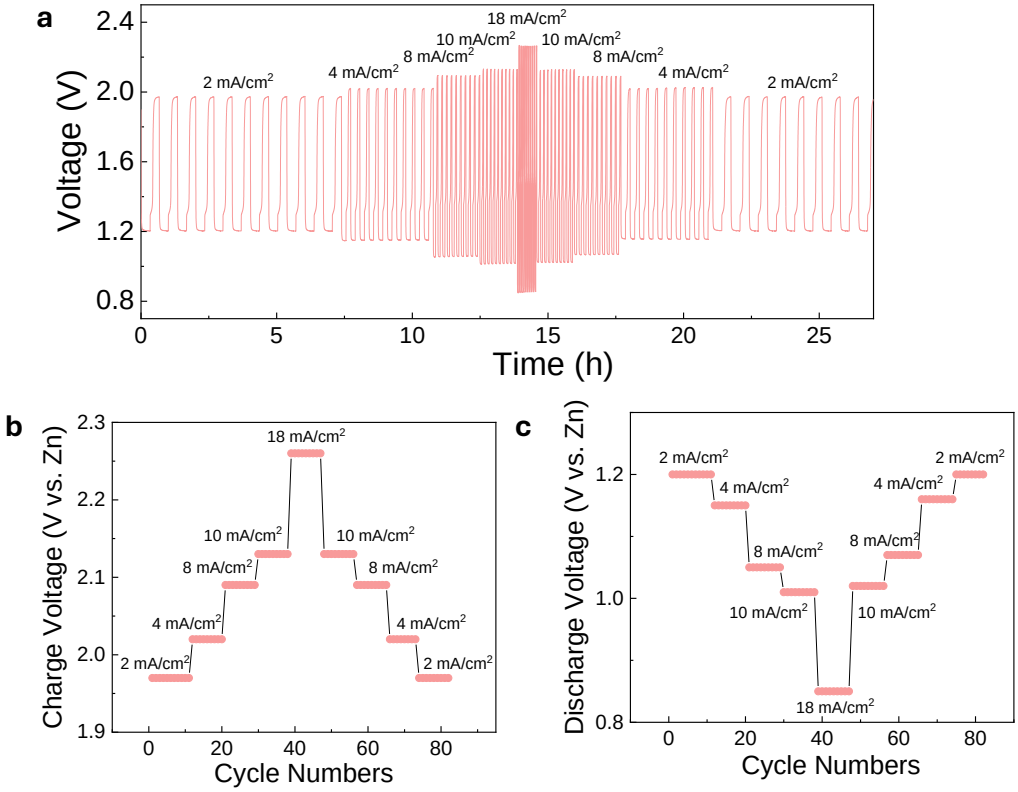

Fig. S56. Rate performance of FeCoNiPdWP-based ZABs. (a) Chare-discharge curves, (b) charge voltage, and (c) discharge voltage at different current rates.

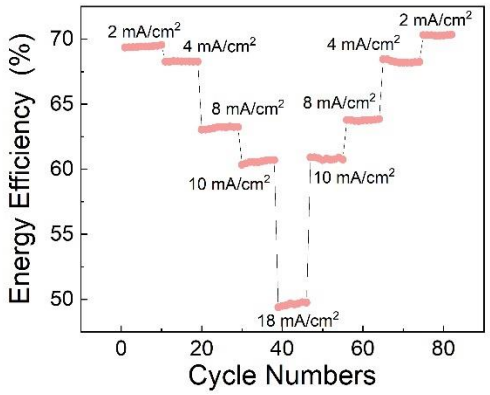

Fig. S57. Energy efficiency of FeCoNiPdWP-based ZABs at different current rates.

Table S1. Parameters obtained from the fitting of the EIS spectra using the equivalent circuit shown in Fig. 2f.

Catalysts	R_s (Ω)	R_{ct} (Ω)
FeCoNiPdWP	5.34	3.96
FeCoNiPdP	4.91	7.92
FeCoPdWP	4.92	14.64
CoNiPdWP	4.81	18.47
FeNiPdWP	4.95	8.27

Table S2. OER performance comparison of FeCoNiPdWP in 1 M KOH with recently reported catalysts on glassy carbon.

Catalyst	*Overpotential@10 mA/cm^2 (mV)*	*Tafel slope (mV/dec)*	*Stability (h)*	*References*
Fe–P/Cu_3P-NPC	350	86	5.56	*Small, 2301985, (2023)*
NiCoFeP	273	35	2000 cycles	*Small, 1802442, (2023)*
Co_2P/CoNPC	326	72.6	8.33	*Adv. Mater.* ***32****, 2003649, (2020)*
CoP@PNC	316	42.9	10000 cycles	*Energy Stor. Mater.,* ***28****, 27-36, (2020)*
NiCoP/C	370	96	10	*Angew. Chem. Int. Ed.,* ***56****, 3897-3900 (2017)*
FeCo/Co_2P @NPCF	330	61	1000 cycles	*Adv. Energy Mater.,* ***10****, 1903854, (2020)*
PdP_2@CB	270	78.6	-	*Angew. Chem. Int. Ed.,* ***57****, 14862 -14867, (2018)*
$Ni_{0.6}Co_{1.4}P$	300	80	10	*Adv. Funct. Mater.,* ***28****, 1706008, (2018)*
NiFeP@NPC	350	78	20	*Appl Catal B-environ,* ***254,*** *292-299, (2019)*
Co_2P	310	50	10	*ACS Energy Lett.,* ***1****, 169–174, (2016)*
Ni_2P	290	47	10	*Energy Environ. Sci.,* ***8****, 2347-2351, (2015)*
Co@CoFe–P	266	26.94	1000 cycles/12	*Energy Environ. Sci.,* ***15****, 727-739, (2022)*
D-CoPHoMSs	294	67	10	*Angew. Chem. Int. Ed.,* ***133****, 7002, (2021)*
NiCoPO/NC	300	94	10	*Nano Energy,* ***69****, 104453, (2020)*
$Co_{0.42}Fe_{0.58}$P@C	262	44.8	20	*Adv. Energy Mater.,* ***12****, 2202394, (2022)*
Fe_0P@C	328	55.1	-	*Adv. Energy Mater.,* ***12****, 2202394, (2022)*
O-CoP	310	83.5	15	*Adv. Funct. Mater.,* ***30****, 1905252, (2020)*
Co-COF-C_4N	280	43	-	*Appl Catal B-environ,* ***325****, 122366, (2023)*
CoNi/Zn(Fe,Al,Cr)$_2O_4$	248	54.7	100	*Adv. Energy Mater., 2303450,*

				(2023)
Co_3O_4-RuO_2-HS	250	55.4	24	*Adv. Funct. Mater.,**32**, 2203206, (2022)*
CeO_2-$CoS_{1.97}$	264	64	50	*Adv. Mater., **33**, 2102593, (2021)*
$Mn_{7.5}O_{10}Br_3$	295	68	500	*Nat. Commun. **13**, 2294, (2022)*
Ag@Co(OH)x/CC	250	76	11	*Angew.Chem. Int. Ed., **59**, 7245-7250, (2020)*
$LiCoO_{1.8}Cl_{0.2}$	270	55	50	*Nat. Catal. **4**, 212, (2021)*
Co/Fe-SNC800	240	48	25	*Energy Environ. Sci., **16**, 1685-1696, (2023)*
CoFe-LDHs	310	59	24	*Nat. Commun., **10**, 1711, (2019)*
Ni SAs/Fe-NiOOH	269	33	11	*Appl Catal B-environ, **297**, 120451, (2021)*
Mo-CoOOH	249	60	36	*J. Mater. Chem. A, **10**, 6242-6250, (2022)*
Ni SAs@S/N-CMF	285	51	60	*Adv. Mater., **34**, e2203442, (2022)*
$N_{i0.9}Fe_{0.1}$-MOF	230	-	150	*Nat. Energy, **5**, 881, (2020)*
Ru-Co/ELCO	247	49	200	*Angew. Chem. Int. Ed. Engl. **61**, e202205946, (2022)*
$Ni_{0.8}Fe_{0.2}$ NSs	230	-	-	*ChemCatChem, **11**, 6002, (2019)*
Co_9S_8/P	230	47.8	-	*Chem. Eng. J. **381**, 122683, (2020)*
WC_x-FeNi	237	44	100	*Nat. Mater. **20**, 1240, (2021)*
CoNC@LDH	240	48	1.38	*Adv. Mater., **33**, 2008606, (2021)*
FeCoNiPdWP	***227***	***33***	***120***	***This work***

NPC: N-, and P- doped carbons, C: Carbon, NPCF: N,P- codoped carbon nanofiber, CB: Carbon black, NC: Nitrogen-doped carbon, @C: @Carbon-cage-encapsulate, HS: Hollow sphere, CC: Carbon cloth, SNC: S,N-codoped carbon, LDHs: Layered double hydroxides, SAs: Single atoms, S/N-CMF: S/N- Doped carbon macroporous fibers, LCO: Layered $LiCoO_2$, NSs: Nanosheets, @LDH: @Layered double hydroxide.

Table S3. Oxidation states from XANES. Bulk oxidation states determined from K-edge XANES data.

K-edge	Before OER	*Reconstructed*
Fe	3.0	3.1
Co	1.4	3.3
Ni	2.0	3.8

Table S4. EXAFS simulations. Tables with the parameters used to simulate the Fe (a), Co (b), Ni (c) K-edge EXAFS data of the as-prepared powder, the as-deposited film, and reconstructed sample by *in situ* freeze-quenching at 1.53 V vs. RHE after 2 h OER operation. R_f represents the fit error sum in % in the range 0-3.5 Å, N the population of the shell at distance R, and σ the Debye-Waller factor. The Debye-Waller factors were fixed in order to diminish the number of variables in the fits. The amplitude reduction factor, S_0^2, was 0.7, 0.8, and 0.9 for Fe, Co, and Ni, respectively. Italic numbers refer to restraint fits with a fixed number of summed-up shell population (Fe *in-situ* sample); bold number refers to a constraint shell population (Co *in-situ* sample). The metal-phosphide and metal-metal distances are consistent with the structure of JCPDS 01-071-0193 $Pd_{15}P_2$. A metal-oxide and additional metal-metal shell has been added for a layered oxyhydroxide structure and is described in the main text. The errors of the fit parameters correspond to the 68 %, 1-sigma, confidence intervals coming from the covariance matrix of the Levenberg-Marquardt fit.

(a) Fe

Powder

Shell	*N*	Error	*R* [Å]	Error [Å]	*σ* [Å]
Fe-O	3.9	0.4	1.94	0.01	0.050
Fe-P	1.5	0.3	2.25	0.01	0.050
Fe-Fe	1.4	0.6	2.66	0.02	0.050
Fe-Fe	1.7	0.7	2.87	0.02	0.050
Fe-P	3.9	0.9	3.22	0.02	0.050
R_f = 9.8					

As-deposited

Shell	*N*	Error	*R* [Å]	Error [Å]	*σ* [Å]
Fe-O	3.5	0.4	1.93	0.01	0.050
Fe-P	1.7	0.3	2.25	0.01	0.050
Fe-Fe	1.2	0.6	2.66	0.02	0.050
Fe-Fe	1.5	0.7	2.86	0.02	0.050
Fe-P	3.6	0.9	3.21	0.02	0.050

			R_f = 9.1		

Rconstructured

Shell	*N*	Error	*R* [Å]	Error [Å]	*σ* [Å]
Fe-O	*3.2*	*0.8*	1.89	0.03	0.050
Fe-O	*2.8*		2.02	0.04	0.050
Fe-Fe	2.2	0.8	2.85	0.03	0.050
Fe-Fe	0.8	0.7	2.98	0.09	0.050
Fe-O	3.0	1.7	3.43	0.05	0.050
			R_f = 9.4		

(b) Co

Powder

Shell	*N*	Error	*R* [Å]	Error [Å]	*σ* [Å]
Co-O	2.7	0.7	2.03	0.02	0.050
Co-P	1.0	0.5	2.26	0.03	0.050
Co-Co	0.9	0.3	2.55	0.02	0.050
Co-Co	1.0	0.3	2.97	0.03	0.050
Co-P	1.5	0.7	3.33	0.04	0.050
			R_f = 11.3		

As-deposited

Shell	*N*	Error	*R* [Å]	Error [Å]	*σ* [Å]
Co-O	2.8	0.7	2.03	0.02	0.050
Co-P	1.1	0.5	2.25	0.03	0.050
Co-Co	1.0	0.3	2.56	0.02	0.050
Co-Co	1.0	0.3	2.97	0.03	0.050
Co-P	1.4	0.7	3.34	0.04	0.050
			R_f = 11.5		

Rconstructured

Shell	*N*	Error	*R* [Å]	Error [Å]	*σ* [Å]
CO-O	**6**		1.89	0.01	0.050
Co-Co	4.3	0.2	2.82	0.01	0.050
Co-O	4.2	1.3	3.40	0.02	0.050
			R_f = 9.2		

(c) Ni

Powder

Shell	*N*	Error	*R* [Å]	Error [Å]	*σ* [Å]
Ni-O	2.5	0.5	2.03	0.02	0.050
Ni-P	1.4	0.3	2.29	0.02	0.050
Ni-Ni	0.6	0.2	2.56	0.02	0.050
Ni-Ni	0.3	0.2	2.92	0.05	0.050
Ni-P	1.0	0.5	3.22	0.04	0.050
R_f = 16.5					

As-deposited

Shell	*N*	Error	*R* [Å]	Error [Å]	*σ* [Å]
Ni-O	2.6	0.5	2.02	0.02	0.050
Ni-P	1.4	0.3	2.29	0.02	0.050
Ni-Ni	0.7	0.2	2.55	0.02	0.050
Ni-Ni	0.3	0.2	2.92	0.04	0.050
Ni-P	1.1	0.5	3.21	0.03	0.050
R_f = 16.5					

Rconstructured

Shell	*N*	Error	*R* [Å]	Error [Å]	*σ* [Å]
Ni-O	4.0	0.3	1.88	0.01	0.050
Ni-Ni	3.3	0.2	2.81	0.01	0.050
Ni-O	2.6	1.1	3.41	0.03	0.050
R_f = 10.4					

Table S5. ORR performance comparison of FeCoNiPdWP with recently reported catalysts.

Catalyst	*Halfwave potential (V vs. RHE)*	*Stability*	*References*
Fe–P/Cu_3P-NPC	0.84	10000 s	*Small, 2301985, (2023)*
FeP/Fe_2P-NPC	0.79	-	*Small, 2301985, (2023)*
Co_2P/CoNPC	0.84	-	*Adv. Mater., **32**, 2003649, (2020)*
CoP@PNC	0.803	10000 cycles	*Energy Stor. Mater., **28**, 27–36, (2020)*
CoP-DC	0.81	5000 cycles	*Adv. Energy Mater., **8**, 1703623, (2018)*
FeCo/Co_2P@ NPCF	0.79	43200 s	*Adv. Energy Mater., **10**, 1903854, (2020)*
V-Fe_2P/$FePO_x$@PG	0.84	12 h	*Appl. Catal. B-environ., **331,** 122674, (2023)*
Ni_xP-NP-C900	0.76	3000 cycles	*Appl. Catal. B-environ., **321,** 122041, (2023)*
NPO/Ni_xP_y@NF-HPCs	0.81	30 h	*Chem. Eng. J., **461**, 141843, (2023)*
Co_2N/CoP@PNCNTs	0.85	3000 cycles	*Small, **18**, 2108094, (2022)*
CoP_3/CeO_2/C-2	0.752	5000 cycles	*Appl. Catal. B-environ., **321,** 122029, (2023)*
CoP	0.858	30 h	*Adv. Mater., **30**, 1705796, (2018)*
FeNiP/NPCS	0.84	10 h	*Chem. Eng. J., **389**, 124408, (2020)*
FeNiCo@NC-P	0.84	5.56 h	*Adv. Funct. Mater., **30**, 1908167, (2020)*
CoNC SAC	0.86	-	*Sci. Adv. **8**, eabn5091, (2022)*
Sb SAC	0.86	5000 cycles	*Angew. Chem. Int. Ed. Engl. **60**, 21237, (2021)*
Fe/SNCFs-NH3	0.89	6000 cycles	*Adv. Mater. **34**, 2105410, (2022)*
Meso-Fe-N-C	0.84	10 h	*ACS Catal. **11**, 74, (2020)*
Pd/C	***0.82***	***-***	***This work***
FeCoNiPdWP	***0.81***	***5000 cycles***	***This work***

Table S6. E_{gap} comparison of FeCoNiPdWP with recently reported excellent bifunctional oxygen catalysts.

Catalyst	*E_{gap} (V)*	*References*
Fe–P/Cu_3P-NPC	0.74	*Small, 2301985, (2023)*
FeP/Fe_2P-NPC	0.86	*Small, 2301985, (2023)*
Co_2P/CoNPC	0.72	*Adv. Mater., **32**, 2003649, (2020)*
CoP@PNC	0.78	*Energy Stor. Mater.,**28**, 27–36, (2020)*
CoP-DC	0.76	*Adv. Energy Mater., **8**, 1703623, (2018)*
FeCo/Co_2P@ NPCF	0.77	*Adv. Energy Mater., **10**, 1903854, (2020)*
V-Fe_2P/$FePO_x$@PG	0.85	*Appl. Catal. B-environ., **331,** 122674, (2023)*
FeNiCo@NC-P	0.70	*Adv. Funct. Mater., **30**, 1908167, (2020)*
Defective Carbon–CoP	0.76	*Adv. Energy Mater., **8**, 1703623, (2018)*
Co_2P@NPC	0.75	*Energy Environ. Mater., **5**, 515-523, (2022)*
CoNC SAC	0.79	*Sci. Adv. **8**, eabn5091, (2022)*
Co-NB-CSs	0.83	*ACS Nano **12**, 1894–1901, (2018)*
$Ni_{66}Fe_{34}$-NC	0.85	*Appl. Catal. Environ. **274**, 119091 (2020)*
CoNC@FeNi-LDH	0.63	*Adv. Mater., **33**, 2008606, (2021)*
FeCu–N–HC	0.72	*Adv. Funct. Mater., **31**, 2006533, (2021)*
Fe–N–C/NiFe-LDH	0.75	*Energy Environ. Sci.,**9**, 2020, (2016)*
PdC+RuO_2	***0.75***	***This work***
FeCoNiPdWP	***0.65***	***This work***

Table S7. Comparison of the ZAB performances obtained using state-of-the-art air cathodes.

Catalyst & Reference	*OCP (V)*	*Peak power density (mW/cm^2)*	*Specific capacity (mAh/g_{Zn}) @ (mA/cm^2)*	*Cycling durability (h) @ (mA/cm^2)*	*Reference*
Fe–P/Cu_3P-NPC	1.39	70.8	815@ 10	81@2; 27@5	*Small, 2301985, (2023)*
Co_2P/CoNPC	1.43	116	-	60@10	*Adv. Mater.,* ***32****, 2003649, (2020)*
CoP@PNC	-	138.57	730.5@10	175@30	*Energy Stor. Mater.,****28****, 27-36, (2020)*
FeCo/Co_2P@ NPCF	1.44	154	-	107@10	*Adv. Energy Mater.,* ***10****, 1903854, (2020)*
V-Fe_2P/$FePO_x$@PG	1.42	137	642.7@5	600@5	*Appl. Catal. B-environ.,* ***331,*** *122674, (2023)*
Co_2N/CoP@PNCNTs	1.07	-	823.8	150@10	*Small,* ***18****, 2108094, (2022)*
CoP_3/CeO_2/C-2	1.34	150	767.7@5	120@5	*Appl. Catal. B-environ.,* ***321****, 122029, (2023)*
FeNiP/NPCS	1.51	163	783.5@10	180@10	*Chem. Eng. J.,* ***389****, 124408, (2020)*
CoP-NC@NFP	1.44	93	-	200@2	*Chem. Eng. J.,* ***428****, 131115, (2022)*
Co/Co_xM_y +Pt/C	1.43	125	-	166.7@10	*Small,* ***15****, 1901518, (2019)*
CoP_x@CNS	1.40	110	-	130@5	*Angew. Chem. Int. Ed.,* ***59****, 21360-21366, (2020)*
FeNiCo@NC-P	1.36	112	807@10	130@10	*Adv. Funct. Mater.,* ***30****,*

					1908167, (2020)
Co-SAs@NC	1.46	105.3	897@20	85@10	*Angew. Chem. Int. Ed., **58**, 5359, (2019)*
Co/Co–N–C	1.41	132	-	330@10	*Adv. Mater., **31**, 1901666, (2019)*
Fe/OES	1.51	186.8	807@5	130@5	*Angew. Chem. Int. Ed., **132**, 7454, (2020)*
Fe–N–C–rich pyrolysis free COF network	1.41	145	784@5	300@5	*Sci. Adv., **5**, eaaw2322, (2019)*
Ni_xFe_{100x}-NC	1.44	140	765@10	334@10	*Appl. Catal., B, **274**, 119091, (2020)*
Fe-N-C/N-OMC	-	113	711@10	66@10	*Appl. Catal., B, **280**, 119411, (2021)*
Fe-Nx-C	1.49	96.4	641@5	300@5	*Adv. Funct. Mater.,**29**, 1808872, (2019)*
TMB@NiNC	1.47	107	765.6@10	222@10	*Adv. Energy Mater. **13**, 2203002, (2023)*
FeCo/FeCoNi@ NC NTs-HF	1.48	156.2	783@5	240@5	*Appl. Catal., B, **254**, 26-36, (2019)*
NiFeLDH/CFP	-	93.9	800@25	333@5	*Adv. Mater. **32**, 1908488, (2022)*
$CuCo_2S_4$ NSs@N-CNFs	1.46	232	896@25	100@5	*Adv. Sci. **6**, 1900628, (2019)*
Co-NiO NFs	1.45	93	830@5	110@2	*Appl. Catal., B, **250**, 71-77, (2019)*
FeN_4CB	1.44	177	800	220@10	*J Energy Chem. **66**, 514-524, (2022)*
FeCoNiPdWP	***1.60***	***123***	***886@8***	***700@8***	***This work***

References

[1] M. Wilke, G. M. Partzsch, R. Bernhardt, D. Lattard, *Chem. Geol.* **2004**, 213, 71.

[2] H. Dau, P. Liebisch, M. Haumann, Anal. Bioanal. *Chem.* **2003**, 376, 562.

[3] J. J. Rehr, R. C. Albers, *Rev. Mod. Phys.* **2000**, 72, 621.

[4] A. Ankudinov, B. Ravel, Phys. Rev. B - Condens. *Matter Mater. Phys.* **1998**, 58, 7565.

[5] M. Risch, V. Khare, I. Zaharleva, L. Gerencser, P. Chernev, H. Dau, *J. Am. Chem. Soc.* **2009**, 131, 6936.

[6] M. Risch, F. Ringleb, M. Kohlhoff, P. Bogdanoff, P. Chernev, I. Zaharieva, H. Dau, *Energy Environ. Sci.* **2015**, 8, 661.

[7] J. N. Hausmann, S. Mebs, K. Laun, I. Zebger, H. Dau, P. W. Menezes, M. Driess, *Energy Environ. Sci*. **2020**, 13, 3607.

[8] J. N. Hausmann, R. A. Khalaniya, C. Das, I. Remy-Speckmann, S. Berendts, A. V. Shevelkov, M. Driess, P. W. Menezes, *Chem. Commun.* **2021**, 57, 2184.

[9] J. N. Hausmann, S. Mebs, H. Dau, M. Driess, P. W. Menezes, *Adv. Mater.* **2022**, 34, 2207494.

[10] J. N. Hausmann, B. Traynor, R. J.Myers, M. Driess, P. W. Menezes, *ACS Energy Lett.* **2021**, 6, 3567−35713.

[11] J. C. Stewart, D. S. Matthew, J. P. Chris, J. H. Phil, I. J. P. Matt, R. Keith, C. P. Mike, Z Krist-Cryst. *Mater.* **2005**, 220, 567–570.

[12] J. P. Perdew, K. Burke, M. Ernzerhof, *Phys. Rev. Lett.* **1996**, 77, 3865–3868.

[13] J. K. Nørskov, J. Rossmeisl, A. Logadottir, L. Lindqvist, J. R. Kitchin, T. Bligaard, H. Jónsson, *J. Phys. Chem. B* **2004**, 108, 17886–17892.